



## City Research Online

### City, University of London Institutional Repository

---

**Citation:** Monti, A., Omidyeganeh, M., Eckhardt, B. & Pinelli, A. (2020). On the genesis of different regimes in canopy flows: a numerical investigation. *Journal of Fluid Mechanics*, 891, A9. doi: 10.1017/jfm.2020.155

This is the accepted version of the paper.

This version of the publication may differ from the final published version.

---

**Permanent repository link:** <https://openaccess.city.ac.uk/id/eprint/23964/>

**Link to published version:** <https://doi.org/10.1017/jfm.2020.155>

**Copyright:** City Research Online aims to make research outputs of City, University of London available to a wider audience. Copyright and Moral Rights remain with the author(s) and/or copyright holders. URLs from City Research Online may be freely distributed and linked to.

**Reuse:** Copies of full items can be used for personal research or study, educational, or not-for-profit purposes without prior permission or charge. Provided that the authors, title and full bibliographic details are credited, a hyperlink and/or URL is given for the original metadata page and the content is not changed in any way.

---

---

---

City Research Online:

<http://openaccess.city.ac.uk/>

[publications@city.ac.uk](mailto:publications@city.ac.uk)

---

# On the genesis of different regimes in canopy flows: a numerical investigation

Alessandro Monti<sup>1</sup>, Mohammad Omidyeganeh<sup>1</sup>, Bruno Eckhardt<sup>2</sup>  
and Alfredo Pinelli<sup>1</sup>†

<sup>1</sup>School of Mathematics, Computer Science and Engineering, City, University of London,  
EC1V 0HB, London, UK

<sup>2</sup>Fachbereich Physik, Philipps-Universität Marburg, 35032, Marburg, Germany

(Received xx; revised xx; accepted xx)

We have performed fully resolved simulations of turbulent flows over various submerged rigid canopies covering the wall of an open channel. All the numerical predictions have been obtained considering the same nominal bulk Reynolds number (i.e.  $Re_b = U_b H / \nu = 6000$ ,  $H$  being the channel depth and  $U_b$  the bulk velocity). The computations directly tackle the region occupied by the canopy by imposing the *zero-velocity* condition on every single stem, while the outer flow is dealt with a highly resolved *Large-Eddy Simulation*. Four canopy configurations have been considered. All of them share the same in-plane solid fraction while the canopy to channel height ratios have been selected to be  $h/H = (0.05, 0.1, 0.25, 0.4)$ . The lowest and the highest values lead to flow conditions approaching the two asymptotic states that in literature are usually termed *sparse* and *dense* regimes (see Nepf 2012). The other two  $h/H$  selected ratios are representative of *transitional* regimes, a generic category that incorporates all the non-asymptotic states. While the interaction of a turbulent flow with a filamentous canopy in the two asymptotic conditions is relatively well understood, not much is known on the transitional flows and on the physical mechanisms that are responsible for the variations of flow regimes when the canopy solidity is changed. The effects of the latter on the flow developing in the intra-canopy region, on the outer flow and on their mutual interactions have been numerically explored and are reported in this work. By systematically varying the canopy height, we have unravelled the main character of the different regimes that are generated by the interplay between the outer flow structures, the emerging instabilities driven by the canopy drag and the interstitial flow between the canopy stems. The key role played by the relative positions of the inflection points of the mean velocity profile and the location of the virtual wall origin (as seen from the outer flow) is put forward and used to define a new condition to infer the canopy flow regime when the solidity is changed. Finally, the presence and the effects of an instability occurring close-to-the-bed, nearby the interior inflectional point of the mean velocity profile is highlighted together with its consequences on the flow structure within the canopy region. To the best of our knowledge, this is the first time that the emergence of close-to-the bed coherent structures induced by the inner inflection point is reported in literature.

## 1. Introduction

Surfaces covered by arrayed, filamentous layers anchored to a substrate and exposed to viscous flows are commonly found in nature, and increasingly seen in bio-inspired technology (Mars *et al.* 1999; Ghisalberti & Nepf 2002; Luhar *et al.* 2008; Wilcock *et al.*

† Email address for correspondence: alfredo.pinelli.1@city.ac.uk

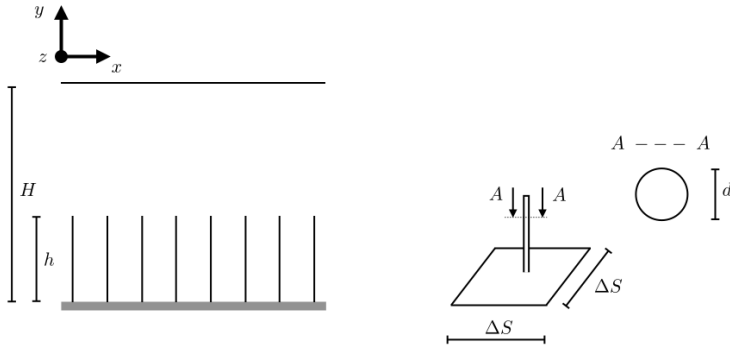


Figure 1: Geometrical parameters governing a canopy flows according to Nepf (2012). In our simulation, the filaments are randomly distributed on the canopy bed, each one occupying an average area  $\Delta S^2$ .

1999). Living organisms use surfaces with complex texture and their interaction with surrounding fluid flows for a number of tasks: decrease skin friction drag (e.g. seal fur, see Itoh *et al.* 2006), control of flight aerodynamics (e.g. birds feathers, see Brücker & Weidner 2014), increase nutrient and light uptake (e.g. vegetative canopies, see Finnigan 2000), form-drag control via reconfiguration (e.g. tree foliage, see Leclercq & de Langre 2016). Ciliated walls and flagella are also commonly found in living organs participating in a number of physiological processes like locomotion, digestion, circulation, respiration and reproduction (see any cellular biology textbook, e.g. Lodish *et al.* 2007).

All the mentioned examples clearly show that the geometrical configuration and the mechanical properties of the various filamentous surfaces found in nature conform to the task that needs to be tackled. Thus, the number of free parameters that define a specific type of ciliated layer, or of a specific canopy is quite large (e.g. density ratios, flexibility, aspect ratios, sizes, level of submersion, active or passive motions, ...) and to incorporate all of them in a comprehensive parametric investigation is an almost impossible task. Here, as in many other previous research efforts, we will focus only on a reduced set of canopy flows where the solidity of the layer is the only feature that differentiates every single realisation. This choice aligns with recent investigations on aquatic plants carried out by Nepf (2012) and collaborators that used a classification of canopy-flows based on only two geometrical properties. The first one is the ratio between the flow depth  $H$  and the canopy height  $h$  (i.e. the *level of submersion*, see Figure 1), to classify canopies as *emergent* ( $H/h = 1$ ), *shallow submerged* ( $1 < H/h < 5$ ) and *deeply submerged* ( $H/h > 10$ ). This definition allows us to classify canopy flows according to the relative importance between turbulent stresses and the flow-driving pressure gradient (Nepf & Vivoni 2000).

In emergent canopies, the turbulence length scale is imposed either by the stem diameter  $d$  or by the average spacing between filaments  $\Delta S$  when the latter is smaller than the former (Nepf 2012). The momentum equation for emergent canopy flows reduces to a balance between the drag force and the driving pressure gradient, leading to a self-similar velocity profile which only depends on the ratio  $a(y)$  between the frontal area  $dh$  and the canopy volume of influence  $\Delta S^2 h$  (Lightbody & Nepf 2006), i.e.  $a(y) = d(y)/\Delta S^2$ .

Submerged canopies substantially differ from the emergent ones as they feature different regimes whose individual genesis depends on a large number of parameters. A key one is the canopy solidity, defined as the ratio between the frontal area of the canopy

and the bed area,

$$\lambda = \int_0^h a(y) dy. \quad (1.1)$$

It is known that for extreme values of  $\lambda$  the flow reaches two asymptotic regimes (Poggi *et al.* 2004; Nepf 2012). If  $\lambda$  is much smaller than a threshold value (i.e.  $\lambda \ll 0.1$ ) then the flow velocity within and above the canopy shows a behaviour comparable to the one observed in a turbulent boundary layer over a rough wall with a dominance of bed drag over canopy form drag (a condition termed *sparse regime*). Conversely, for large values of  $\lambda$  (i.e.  $\lambda \gg 0.1$ ), the drag produced by the bed becomes negligible when compared to the canopy one. In this situation, termed *dense regime*, the drag discontinuity at the tip of the canopy induces the appearance of an inflection point in the mean velocity profile at the canopy edge. Another, often overlooked, inflection may form closer to the bed, where the boundary layer at the wall merges with the mean profile that develops in the core of the canopy.

In a dense regime, these two inflection points divide the intra-canopy flow into separate regions: an inner region, very close to the bed, an outer region, mostly located outside the canopy, and a central region sandwiched between the two. Within this mid-portion of the canopy, it can be assumed that a peculiar *Couette* flow takes place with a large portion of the short-wavelength fluctuations produced by the meandering of the flow in between the canopy elements. This conceptual, three layers structure of dense canopy flows has been firstly proposed by Belcher *et al.* (2003).

Poggi *et al.* (2004) carried out an experimental campaign on rigid canopy flows in which they varied the canopy density (the number of stems per unit bed surface, i.e.  $\Delta S^2$ ). They were able to show that the mean velocity profile does not present a clear inflection point at the canopy edge for values of  $\lambda < 0.04$  (i.e. within the *sparse regime*). Conversely, when  $\lambda > 0.1$ , the mean velocity profile clearly featured a pronounced inflection point at the tip of the canopy layer in agreement with the observations of Nepf (2012). Poggi *et al.* (2004) also proposed a phenomenological classification for canopy flows: in the sparse regime, the flow is assumed to behave like a boundary layer over a rough wall, while in the dense regimes, the flow can be modelled using a weighted superposition of three distinct zonal flow behaviours determined by the size of the largest eddy that can be locally accommodated. Following the spirit of classical Prandtl's mixing layer models, each zone was assumed to set a different length scale. Specifically, in the canopy inner region, i.e.  $y/h \ll 1$ , the flow field is assumed to be characterised by vortices shed by the canopy elements whose size and intensity depend on the diameter of the stems. Supported by the observations of other authors (Raupach *et al.* 1996; Finnigan 2000), the outer region, i.e.  $y/h \gg 2$ , is postulated to behave like a classical boundary layer over a rough wall. Finally, within the region overlapping the innermost and outermost zones, the flow is assumed to be dominated by a mixing-layer of constant thickness.

The formation of a mixing-layer flow by the canopy edge is induced by the inflected mean velocity profile that triggers a Kelvin-Helmholtz (KH)-like instability. The latter eventually leads to large scale spanwise vorticity rollers. The size of these structures is comparable to the height of the canopy for unsaturated regimes: i.e. whenever the thickness of the filamentous layer is short enough for the outer flow to be conditioned by the presence of the impermeable, bottom wall (coarse to marginally-dense regimes). This system of spanwise vortices, that is believed to govern the bulk of the momentum transport between the outer and the inner region in dense canopies (Nepf 2012), has also been reported by other authors in other contexts (for example, in turbulent wall flows over porous media, see Jiménez *et al.* 2001). Raupach *et al.* (1996) observed that within

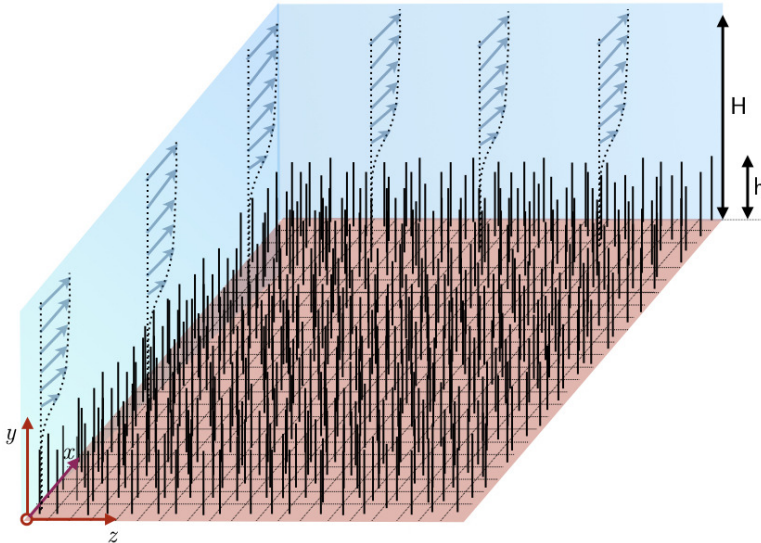


Figure 2: Sketch of the computational domain. The bottom wall of the open channel is covered with a uniform distribution of square tiles with an area  $\Delta S \times \Delta S$ . On each tile, a stem is mounted orthogonally at a location that is randomly chosen. In the figure,  $H$  is the open channel depth, while  $h$  is the height of the stems. The bulk flow is driven along the  $x$  direction. Also,  $y$  is the wall-normal coordinate and  $z$  is the spanwise direction.

the developed mixing-layer near the canopy tip, the most unstable streamwise wavelength of the KH instability,  $\Lambda_x$ , is spatially preserved. Moreover, they also suggested that the ratio between  $\Lambda_x$  and the mixing layer vorticity thickness  $\delta_\omega = \Delta U / (\partial U / \partial y)_{max}$  falls within the range,  $3.5 < \Lambda_x / \delta_\omega < 5$  (Finnigan 2000). The same authors (Raupach *et al.* 1996) also showed that for dense canopies, the ratio between the KH most unstable wavelength and a measure of the vorticity thickness  $L_s = U(h) / \partial_y U(h)$ , obtained by considering the velocity gradient at the canopy tip only, is found to be within the range  $7 < \Lambda_x / L_s < 10$ . Indeed, several experiments have confirmed this bound and have put forward an even more stringent relation given by  $\Lambda_x \simeq 8.1 L_s$ . Another three-layers model for dense submerged canopies, similar to the one put forward by Poggi *et al.* (2004), has been proposed by Nezu & Sanjou (2008). They conjectured that the flow behaviour within each layer develops as a consequence of a single dominant generation mechanism enhancing the observed local features while inhibiting the coexistence of other vorticity structures pertaining to neighbouring layers.

The bibliographic survey that has been presented above is just a limited sample of the large body of literature addressing submerged canopies. The main research tool behind the majority of these studies is of experimental nature, thus limited by the presence of the filamentous canopy that renders the use of localised measurements difficult (e.g. laser Doppler velocimetry - LDV - or particle image velocimetry - PIV). Despite these limitations, the literature presents an increasing proliferation of canopy-flow models that need verification and validation through techniques that can provide more detailed insight into the flow fields arising in canopy flows. In particular, the determination of proper scaling and of robust criteria able to deliver an a priori prediction on the insurgence of particular canopy flow regimes are still open topics and available analysis and predictions only cover specific situations. Moreover, the condition for the emergence of different intra-canopy flows at intermediate flow regimes and their detailed characterisation are

still not well documented, let alone the understanding of the interplay between physical mechanisms as the flow transitions from one regime to another. This lack of understanding is particularly evident in the *transitional* regime scenario where the main features of the *coarse* and *dense* regime combine in a non-trivial way. As it will be shown in the results section, this regime establishes when the positions of the virtual wall seen by the outer flow and the innermost mean velocity inflection point cross. In physical terms, the transition between the two asymptotic regimes corresponds to the formation of a central region in the canopy where the outer flow overlaps with the portion of the flow developing in the region close to the bottom wall. Other potentially relevant mechanisms that has not been considered in-depth concern the role of KH-generated spanwise vorticity rollers, their modification by the outer flow structures and their role in redistributing the local momentum within and outside the canopy (Monti *et al.* 2019).

Without pretending to offer a final say on general canopy flows and only by varying the frontal solidity of the canopy  $\lambda$ , the research presented in this work addresses some of the mentioned research topics where no reliable or validated understanding is available. In particular, through the analysis of the flows arising when changing the canopy solidity  $\lambda$ , we will identify the dominant scales of motions that are either enhanced or weakened in different regimes. This understanding allows us to establish a robust macroscopic criterion able to predict the dominant features of canopy flows when  $\lambda$  is varied. The latter, is based on the relative positions of the inflection points of the mean velocity profile and the virtual origin seen by the outer flow.

The approach that we have considered to tackle those questions relies on the analysis of a set of highly resolved simulations of a turbulent flow in an open channel bounded by rigid canopies of various solidity, assembled with vertically-mounted filaments. The value of  $\lambda$  is set within a range of values that generate canopy flows nominally varying from *sparse* to *dense* regimes. In particular, we report results obtained using a formulation that directly resolves the intra-canopy flow stem-by-stem by imposing a zero velocity condition on each element of the filamentous layer. The manuscript is organised as follows. Section §2 describes the numerical method used to undertake the simulations. Section §3 describes the obtained results. Their analysis is mainly carried out by comparing the statistical and instantaneous characterisations of the canopy flow fields realised with four different values of the solidity  $\lambda$ . Finally, Section §4 outlines the most important conclusions with emphasis on the new findings that mainly concern the introduction of a generalised scaling approach for the mean flow statistical values, a novel criterion to predict the canopy flow regime and new observations on the flow structure of the close-to-the-bed intra-canopy region which is strongly influenced by the internal mean velocity inflection point.

## 2. The numerical technique

We have simulated the turbulent flows over rigid canopies using an incompressible Navier-Stokes solver developed in-house (SUSA, Omidyeganeh & Piomelli 2013a). In particular, we adopted a Large-Eddy Simulation (LES) formulation where the governing equations are obtained from the full Navier-Stokes equations by filtering out the velocity and pressure fluctuations taking place on all length scales smaller than a spatial filter which width falls within the inertial range of turbulence. In a Cartesian frame of reference, indicating with  $x_1$ ,  $x_2$  and  $x_3$  (i.e.  $x$ ,  $y$  and  $z$ ) the streamwise, wall-normal and spanwise directions and with  $u_1$ ,  $u_2$  and  $u_3$  the corresponding velocity components (i.e.  $u$ ,  $v$  and  $w$ ), the dimensionless incompressible LES equations for the resolved fields  $\bar{u}$  and  $\bar{p}$  read

---

Nominal regime	Canopy height $h/H$	Solidity $\lambda$	Case	Symbol
<i>Marginally Sparse</i>	0.05	0.07	<i>MS</i>	○
<i>Transitional</i>	0.10	0.14	<i>TR</i>	▽
<i>Marginally Dense</i>	0.25	0.35	<i>MD</i>	□
<i>Dense</i>	0.40	0.56	<i>DE</i>	+

---

Table 1: Considered canopy configurations: nominal regimes (Nepf 2012), canopy height and solidity, and corresponding acronyms and symbols. Note that we have used a total of  $48 \times 36$  stems. All tiles, where the stems are mounted on the bed, are identical squares with an edge of  $\Delta S \simeq 0.13 H$ .

---

as

$$\frac{\partial \bar{u}_i}{\partial t} + \bar{u}_j \frac{\partial \bar{u}_i}{\partial x_j} = -\frac{\partial \bar{P}}{\partial x_i} + \frac{1}{Re_b} \frac{\partial^2 \bar{u}_i}{\partial x_j \partial x_j} + \frac{\partial \tau_{ij}}{\partial x_j} + f_i, \quad \frac{\partial \bar{u}_i}{\partial x_i} = 0. \quad (2.1)$$

In (2.1),  $Re_b = U_b H / \nu$  is the Reynolds number based on the bulk velocity  $U_b$ , the open channel height  $H$  and  $\nu$  is the kinematic viscosity.  $\tau_{ij} = \overline{u_i u_j} - \bar{u}_i \bar{u}_j$  is the subgrid Reynolds stress tensor (Leonard 1975) that was modelled using the Integral Length-Scale Approximation (ILSA) approach recently proposed by Piomelli *et al.* (2015) (see also Rouhi *et al.* 2016). The incompressible LES equations (2.1) are space-discretised using a second-order accurate, cell centred finite volume method. Pressure and velocity are co-located at the centres of the cells and the approach of Rhie & Chow (1983) is used to avoid pressure oscillations. The equations are advanced in time using a second-order, semi-implicit fractional-step procedure (Kim & Moin 1985). In particular, the implicit Crank-Nicolson scheme is implemented for the wall-normal diffusive terms while an explicit Adams-Bashforth scheme is applied to all other terms. The Poisson pressure equation, that needs to be solved at each time step to enforce the solenoidal condition of the velocity field, is transformed into a series of two-dimensional (2D) Helmholtz equations in the wavenumber space using a Fast Fourier Transform (FFT) along the spanwise direction. Each of the resultant elliptic 2D problems is then solved using a preconditioned Krylov method. In particular, we found the iterative Biconjugate Gradient Stabilized (BiCGStab) method with an algebraic multigrid preconditioner (*boomerAMG*, see Yang *et al.* 2002) to behave quite efficiently. The code is parallelised using the domain decomposition technique implemented via the MPI message passing library. Further details on the code, its parallelisation and the extensive validation campaign, that had been carried out in other flow configurations, can be found in previous publications (Omidyeganeh & Piomelli 2011, 2013*a,b*; Rosti *et al.* 2016).

Unlike other approaches (e.g. Bailey & Stoll 2016), our formulation can be considered as a *coarse* Direct Numerical Simulation (DNS) in the outer portion of the flow that progressively becomes highly resolved as the canopy is approached. In the outer flow region, the subgrid stress contribution plays only the role of a very mild and stabilising numerical dissipation. Indeed, the ratio between the total and the subgrid energies averaged in time and in the two homogeneous directions, shown in the left panel of Figure 3 along the channel height, is always below  $10^{-5}$  for all the canopy configurations. A further indication that the LES filter operates at the end of the turbulence cascade is provided in the right panel of Figure 3 showing that the ratio between the time and space averaged eddy viscosity and the physical one is always of order unity or less throughout the whole channel for all the considered stems distributions. In the intra-

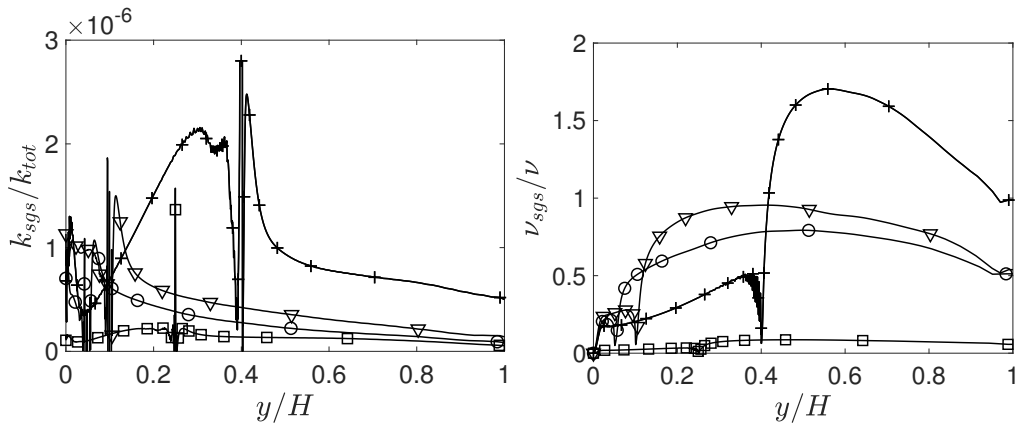


Figure 3: Left panel: ratio between the sub-grid energy and the total fluctuating energy in the wall-normal direction. Right panel: ratio between the eddy viscosity and the physical viscosity along the channel height. In both panels the quantities have been averaged in time and in both spatial homogeneous directions. Symbols as in Table 1.

canopy region, we resolve the canopy stems one by one without the introduction of any model. In particular, the stems embedded in the canopy are represented as rigid, solid, slender cylindrical rods of finite cross-sectional area perpendicularly mounted onto the impermeable bottom wall. To enforce the boundary conditions that each rigid cylinder imposes on the fluid (i.e., zero-velocity at the surface of each stem) we used an immersed boundary method (IBM). The latter deals with the presence of the rods, whose locations do not conform with the actual fluid grid, by using a set of nodes distributed along the length of each canopy element (termed *Lagrangian nodes*). More specifically, the employed IB method associates to each Lagrangian node a set of distributed body forces defined on a compact support centred on each node. At each time step, the intensity of those forces is determined by enforcing a Dirichlet condition, i.e. zero-velocity of the fluid, on all the nodes used to discretise each element of the canopy. The size of the support is related to the local grid size and also defines the hydrodynamic thickness of the filament that in our case can be estimated to be  $2.2 \Delta x$  (Monti *et al.* 2019), or  $2.2 \Delta z$ , since the mesh spacing is the same in the  $x$  and  $z$  directions. The adopted immersed boundary method and its properties are described and discussed in Pinelli *et al.* (2010) and in Favier *et al.* (2014). The assessment of the immersed boundary method, including the calibration of the support of each Lagrangian node required to deliver a resolution comparable to an *interface resolved* immersed boundary formulation (Fadlun *et al.* 2000) can be found in Monti *et al.* (2019). In particular, in the given reference we show that although the details of the boundary layers forming on each stem cannot be properly captured, the wake structure and the drag on each stem is very well predicted. To distribute the stems on the bottom wall, we have subdivided the latter in a Cartesian lattice of uniform squares of area  $\Delta S^2$  (see Figure 1 and Table 1). Each filament has been attached orthogonally to each square-shaped tile, with its local positioning determined according to a uniform random distribution. The use of a random assignment on each tile prevents eventual flow channelling effects within the canopy, i.e. preferential flow corridors, or repeating, ordered flow patterns as in a staggered configuration. A sketch of the computational domain that includes the distribution of the stems on the channel bottom wall is shown in Figure 2. The tile size and the filament height  $h$  can be adjusted to match any solidity value  $\lambda$ , defined in (1.1). For stems with a uniform cross-sectional

---

Case	Spacing at $y = 0$	Spacing at $y = h$	Spacing at $y = H$
<i>MS</i>	$\Delta y = 10^{-3} H$	$\Delta y = 7.0 \times 10^{-4} H$	$\Delta y = 3.2 \times 10^{-2} H$
<i>TR</i>	$\Delta y = 10^{-3} H$	$\Delta y = 5.0 \times 10^{-4} H$	$\Delta y = 2.0 \times 10^{-2} H$
<i>MD</i>	$\Delta y = 10^{-3} H$	$\Delta y = 3.0 \times 10^{-4} H$	$\Delta y = 2.3 \times 10^{-2} H$
<i>DE</i>	$\Delta y = 10^{-3} H$	$\Delta y = 2.5 \times 10^{-4} H$	$\Delta y = 2.0 \times 10^{-2} H$

---

Table 2: Details on the nodes distribution in the wall-normal direction for the four simulated canopies. Note that for cases *MS* and *TR* the  $\max(\Delta y_{j+1}/\Delta y_j) \leq 1.03$ ,  $\forall j$ , while for cases *MD* and *DE* the  $\max(\Delta y_{j+1}/\Delta y_j) \leq 1.04$ ,  $\forall j$ .

---

circular area of diameter  $d$ , the solidity simply reads as

$$\lambda = \frac{d h}{\Delta S^2} = \frac{d}{h} \cdot \left( \frac{h}{\Delta S} \right)^2. \quad (2.2)$$

The results that will be presented correspond to values of  $\lambda$  obtained by keeping constant the tiles and the stems cross-sectional areas (i.e.  $\Delta S$  and  $d$  in (2.2)), whilst varying the height  $h$  of the canopy (i.e. all stems share the same height  $h$ ). In particular, in (2.2) we have set  $\Delta S/d \approx 5.5$  and selected four canopy heights or, equivalently four  $\lambda$  values, that nominally lead to the emergence of different canopy-flow regimes (Nepf 2012), as detailed in Table 1.

The four cases share the same computational box of size  $L_x/H = 2\pi$ ,  $L_y/H = 1$  and  $L_z/H = 3/2\pi$ , similar to the one used by Bailey & Stoll (2013) for the case of a nominally dense canopy flow regime. The numerical domain is set to be periodic in both the streamwise (i.e.  $x$ ) and the spanwise (i.e.  $z$ ) directions. The choice of selecting a streamwise periodic condition, even for the densest case, is motivated by the experiments of Ghisalberti & Nepf (2004) whose observations highlighted the presence of a mixing layer nearby the canopy edge that preserved its thickness in the streamwise direction. At the bottom wall, i.e. the canopy bed, a zero-velocity boundary condition is imposed while, at the top surface, a free slip condition is set to mimic an open channel free surface.

The four simulations have been carried out using a Cartesian grid with a uniform distribution in the  $x$  and  $z$  directions, and with a mildly stretched distribution of the nodes in the bed-normal direction. While the grid on every  $x - z$  plane has been kept the same for the four simulations, the wall-normal distribution has been adjusted to adapt to the variations of the height of the stems. The number of nodes in the  $x$  and  $z$  directions is set to  $N_x = 576$  and  $N_z = 432$ , respectively. In the  $y$ -direction, the number of grid points ranges from a minimum value of  $N_y = 180$  for the sparsest case (case *MS* in Table 1), to a maximum of  $N_y = 340$  for the densest canopy (case *DE* in Table 1). With this choice, the  $x$  and  $z$  spacings in wall units inside the canopy are kept below 3, i.e.  $\Delta x_{in}^+ = \Delta x \cdot u_{\tau_{in}}/\nu \leq 3$  and  $\Delta z_{in}^+ = \Delta z_{in}^+ \leq 3$  (note that  $u_{\tau_{in}} = \sqrt{\tau_w/\rho}$ , where  $\tau_w$  is the wall shear stress at the bed, i.e. at  $y = 0$ ). In the portion of the flow outside the canopy, the  $x$  and  $z$  spacings satisfy the inequalities  $\Delta x_{out}^+ = \Delta x \cdot u_{\tau_{out}}/\nu \leq 11$  and  $\Delta z_{out}^+ = \Delta z_{out}^+ \leq 11$ , and are thus well within the standard values suggested for wall-bounded flows (Kim *et al.* 1987). In the previous definitions,  $u_{\tau_{out}}$  is a *friction velocity* determined using the total stress in the  $y$  location corresponding with the *virtual* origin of the outer logarithmic boundary layer (further explanations are provided in the next section and in Monti *et al.* 2019). Concerning the grid spacings along the  $y$ -direction, two tangent hyperbolic distributions have been used inside and outside the canopy ensuring

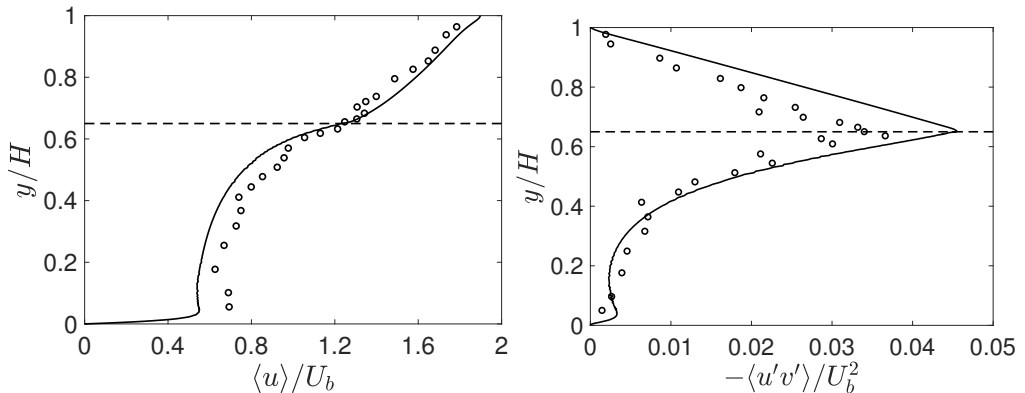


Figure 4: Left panel: comparison of the predicted mean velocity profile (solid line) with the experimental values R31 of reference (Shimizu *et al.* 1991) (dotted curve). Right panel: Reynolds shear-stress distribution predicted versus the experimental value R31 (Shimizu *et al.* 1991). The dashed line represents the location of the canopy tip at  $y = h$ .

that the ratio between neighbouring cells in the interval  $[0, h] \cup [h, H]$  is kept below 4%. Table 2 details the adopted grid spacings inside and outside the canopy along the wall-normal direction. Further discussion on the suitability of the numerical scheme and on the adopted resolution inside and outside the canopy is provided in Monti *et al.* (2019) where the interested reader will also find a detailed validation campaign based on a comparison with interface resolved numerical simulations and the calibration required to produce reliable results using a diffused interface, immersed boundary method. Finally, concerning the global channel flow equilibrium, a uniform pressure gradient is applied in the streamwise direction. In particular, at each time step, the mean streamwise pressure gradient is adjusted to fix the volumetric flow rate to a constant value corresponding to a bulk Reynolds number of  $Re_b = U_b H / \nu = 6000$ . Although the bulk Reynolds number is not the most important indicator of the nature of the flow (Ghisalberti & Nepf 2004), we have chosen this particular value for being very close to the one used in the experimental work of Ghisalberti & Nepf (2004) and of Shimizu *et al.* (1991). A direct comparison with the last set of experimental data, in particular with their R31 measurements campaign, is provided in Figure 4, showing the mean velocity profile and the Reynolds shear stresses for the same canopy configuration, i.e.  $h/H = 0.65$ ,  $\lambda = 0.83$  and  $Re_b = 7070$ .

### 3. Results

The four different values of  $\lambda$  reported in Table 1 have been used to carry out statistically converged simulations of the respective canopy flows. The results collected in this section will be mainly illustrated by a direct comparison between the statistical quantities and the structures of the four flow fields. In the next sub-section, we will start by considering the mean velocity profiles, whilst the following sub-sections will discuss higher-order statistical distributions and the emergence and disappearance of the coherent structures that characterise and govern the different regions of each canopy flow.

#### 3.1. Mean velocity profiles

We start by considering the effect of  $\lambda$  on the mean velocity profiles. In a non-sparse regime (i.e.,  $\lambda > 0.04$ ), the mean velocity profile of a turbulent canopy flow is known to exhibit two inflection points (Nepf 2012; Poggi *et al.* 2004), one at the edge of the

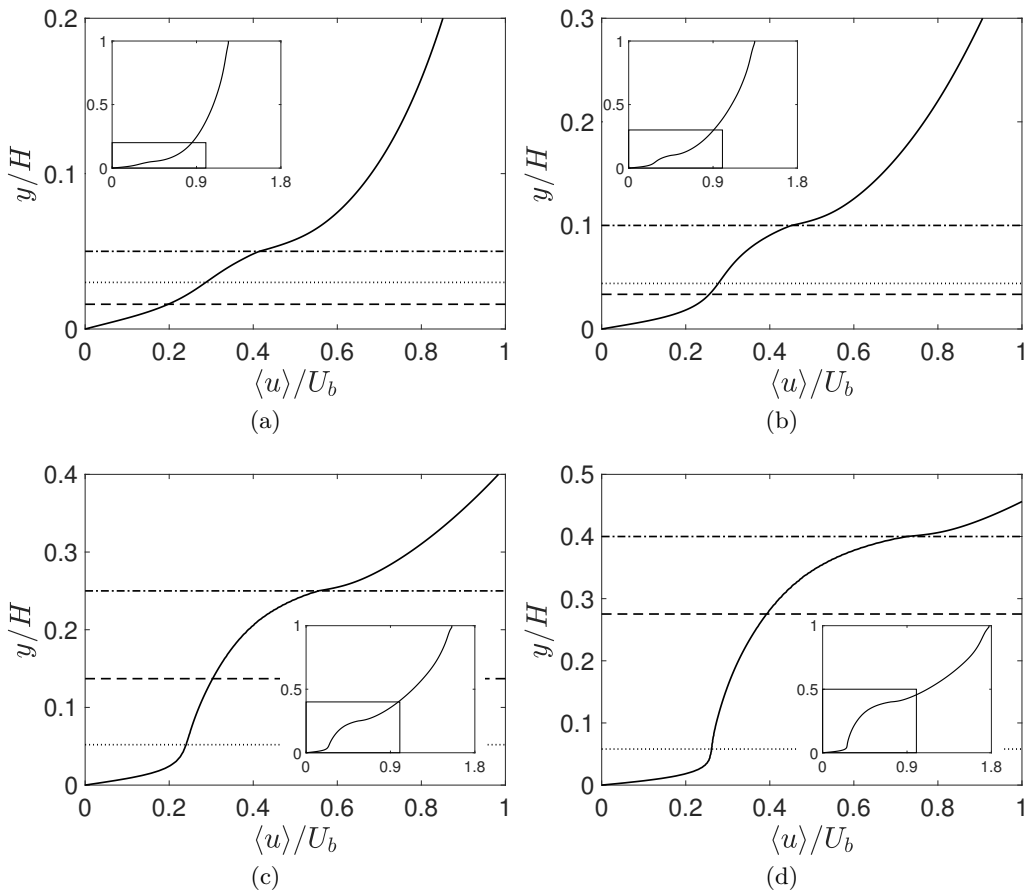


Figure 5: Mean velocity profiles for the four cases. The small frame on the left, top corner of each plot shows an enlarged view. The profiles are ordered left to right, top to bottom according to the  $\lambda$  value of each case: (a) *MS* ( $\lambda = 0.07$  and  $h/H = 0.05$ ); (b) *TR* ( $\lambda = 0.14$  and  $h/H = 0.10$ ); (c) *MD* ( $\lambda = 0.35$  and  $h/H = 0.25$ ); (d) *DE* ( $\lambda = 0.56$  and  $h/H = 0.40$ ). The three lines parallel to the bed indicate: the location of the first inflection point (dotted line), the location of the virtual origin (dashed line) and the location of the canopy height, i.e. the second inflection point (dash-dotted line).

canopy and the other closer to the wall. The mean velocity profiles obtained for the four considered  $\lambda$  values, shown in Figure 5, exhibit this pair of inflection points.

The inflection point at the canopy edge is due to the drag discontinuity arising as a consequence of the sudden end of the stems, while the inner inflection point is a result of the merging of the linear, close-to-the-bed velocity profile with the convex shape of the mean velocity distribution at the canopy tip. The location of the inflection points can be obtained by computing the zeros of the average, streamwise momentum balance,

$$\frac{1}{Re_b} \frac{d^2 \langle u \rangle}{dy^2} = \frac{\partial P}{\partial x} + \frac{d \langle u'v' \rangle}{dy} + \langle D \rangle. \quad (3.1)$$

In the above equation, the symbol  $\langle \ \rangle$  denotes the triple average operator obtained by taking the mean values in time and along the two homogeneous spatial directions,  $x$  and

$z$ . The first term of (3.1) represents the mean viscous force, the second the mean pressure gradient, the third the mean Reynolds shear stress and the last one takes into account the overall mean drag due to the canopy stems which is discontinuous at  $y = h/H$ . The two inflection points enclose a *transitional* zone, where a mixing layer-like flow develops between the innermost and outermost boundary layers (Poggi *et al.* 2004). Along the wall-normal direction, the origins of these two boundary layers are located at the solid wall and just below the canopy tip, respectively. The latter can be interpreted as the location of a virtual wall seen by the outer flow,  $y_{vo}$ . The position of this *virtual origin* can be determined by enforcing the mean outer flow to take on a canonical logarithmic shape, i.e.

$$\langle u \rangle = \frac{u_{\tau,out}}{\kappa} \log \left( \frac{(y - y_{vo})u_{\tau,out}}{\nu} \right) + B. \quad (3.2)$$

The above is one of the standard modifications of the boundary layer *log laws* for flows over rough surfaces (Jiménez 2004). In (3.2),  $\kappa$  is the von Kármán constant and  $u_{\tau}$  is the friction velocity computed using the value of the total stress at the virtual origin  $y_{vo}$ , i.e.  $u_{\tau,out} = (\tau(y_{vo})/\rho)^{1/2}$ , with

$$\tau(y_{vo}) = \mu \left. \frac{d\langle u \rangle}{dy} \right|_{y=y_{vo}} - \rho \langle u'v' \rangle (y_{vo}). \quad (3.3)$$

If the total stress profile is known, the logarithmic law (3.2) can be seen as an implicit equation for the unknown  $y_{vo}$  (for further details see Monti *et al.* 2019).

The virtual origin of the external flow and the locations of the two inflection points of the mean velocity profile of a canopy flow represent a signature of the actual flow regime. In particular, their mutual signed distances define the level and the nature of the interaction between the inner and the outer boundary layers. In our methodology, the canopy becomes sparser as its height  $h$  is shortened leading to a narrower transition zone corresponding to an increase in the size of the overlapping region between the internal and external boundary layers. As the canopy height becomes shorter, the virtual origin asymptotically moves towards the canopy bed and the two inflection points gradually merge, eventually collapsing into a single location. This condition is typical of very sparse canopy regimes (i.e.  $\lambda < 0.04$ ) or, more in general, of turbulent boundary layer flows over *canonical* rough surfaces. Figure 6(a) shows the locations of the two inflection points and of the virtual origin for the four  $\lambda$  cases that we have considered (see Table 1). Note that the location of the virtual origin has been determined by setting the von Kármán constant to  $\kappa = 0.41$  in (3.2). The choice of another  $\kappa$  value within the experimentally credible range  $0.37 \leq \kappa \leq 0.42$  would lead to variations on the coordinate of the virtual origin within a  $0.05 h/H$  margin (see Monti *et al.* 2019). Figure 6(a) shows that, as the height of the canopy is reduced (i.e. reducing the value of  $\lambda$ ), the wall-normal location of the virtual origin moves closer to the bed while the innermost inflection point approaches the canopy tip (i.e. the second inflection point) at  $y = h$ . For the sparsest cases that we have considered (i.e. cases *MS* and *TR* Table 1), the location of the virtual origin is below the inner inflection point indicating that the outer boundary layer has a strong interaction with the intra-canopy flow although the values of  $\lambda$  for the *MS* and the *TR* cases are above the sparse/dense threshold identified by Nepf (2012). More in general, Figure 6(a) indicates that the signed distance between the virtual origin and the inner inflection point is a function of  $\lambda$  that has a zero within the interval  $\lambda \in (0.14, 0.35)$ . We suggest using the value of  $\lambda$  for which the coordinate of the virtual origin coincides with the interior inflection point as a sharp criterion defining the inception of the *dense regime*.

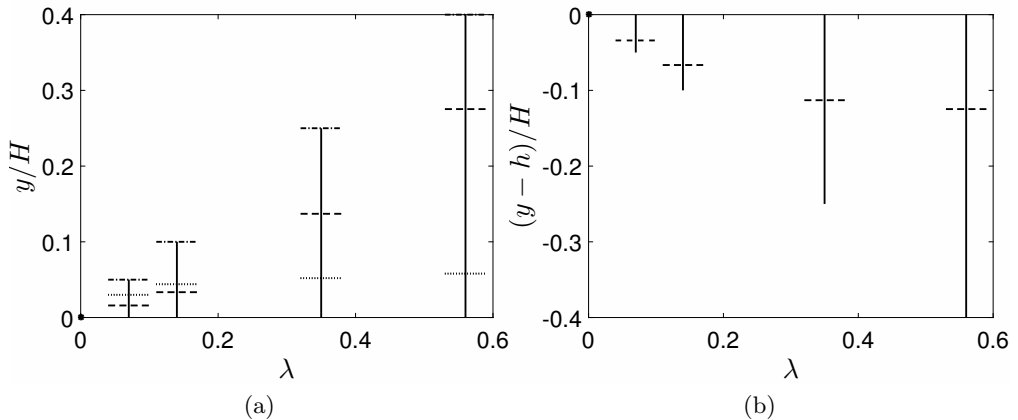


Figure 6: (a) Mean locations of the two inflection points and of the virtual origin along the canopy stem (virtual origin: - - - ; inner inflection point: .....; outer inflection point: - · - ·). (b) Location of the virtual origin in a reference system which zero is set at the canopy tip. Note that the small dot on the left of the horizontal axis (bottom in (a) and top in (b)) represents a flow on a smooth surface (i.e. no-canopy). The vertical continuous lines represent the stems.

Figure 6(b) shows the variations of the distance between the virtual origin and the outer inflection point (i.e. the canopy tip). From the figure, it appears that  $h - y_{vo}$  approaches a constant value as the canopy becomes denser (i.e. increasing the  $\lambda$  value). This asymptotic saturation of the location of the virtual origin corresponds to a decoupling of the outer flow from the inner one: for large values of  $\lambda$ , the outer turbulent flow does not see a wall-bounded canopy but a set of stems whose height becomes progressively independent of  $\lambda$ .

A heuristic model able to explain the variations of the locations of the virtual origin and of the mean profile inflection points as a function of  $\lambda$  can be developed by considering the ratio of the size of the eddies populating the close-to-the-canopy region and the geometric dimensions of the canopy. In particular,  $(\Delta S - d)/h$  (or, equivalently,  $\Delta S/h$  for slender stems where  $d/h \ll 1$ ) defines the magnitude of the in-plane canopy voids as compared to the canopy depth (see Figure 7). If  $\Delta S/h < 1$ , only vortices of diameter  $\phi_{\text{eddy}} < O(\Delta S)$  will be able to fully penetrate the canopy. In this case, the typical length-scale close to the canopy tip is  $\Delta S$  itself (the tips of the stems produce eddies at a length-scale comparable to their spacings) and therefore only eddies with a size  $\simeq \Delta S$  can be hosted in-between the stems (see the sketch in Figure 7). As a consequence, the virtual origin of the canopy seen by the outer flow will saturate close to the edge at a distance from the tip of  $O(\Delta S)$ . The given description is not very dissimilar from the *d-type* roughness scenario proposed by Perry *et al.* (1969) that envisaged a situation in which stable vortices forms in-between roughness elements.

When  $\Delta S/h > 1$ , the mean filaments distance,  $\Delta S$ , does not anymore set an upper bound on the size of the eddies size that can penetrate the canopy. In this case, the distance from the cores of the eddies to the bottom wall determines the allowed depth by which the outer eddies can *leak* into the canopy. In this condition, for sufficiently tall canopies,  $y_{vo}$  becomes a function of  $h/H$  (or  $\lambda$ ), a situation that recalls a *k-type* roughness behaviour (Schultz & Flack 2009).

Using the heuristic argument explained above, we can estimate the value of the canopy

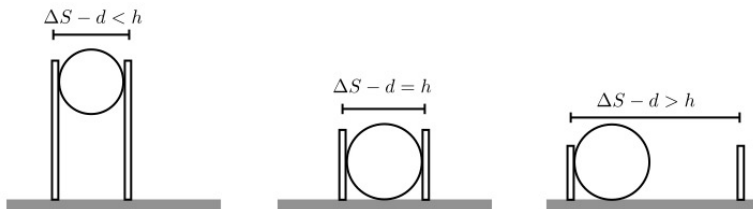


Figure 7: Sketch of the largest vortex size able to penetrate from the outer layer into the canopy. The vortex is represented as a circle with diameter  $\Delta S - d$  or  $h$ .

height for which the virtual origin collapses into the innermost inflectional point (i.e. the condition that we propose to establish the inception of a *dense regime*). This occurs when  $\Delta S - d \simeq h$ :

$$\frac{\Delta S - d}{h} \simeq 1 \rightarrow \frac{h}{H} \simeq (1 - 0.182) \frac{\Delta S}{H} \rightarrow \frac{h}{H} \simeq 0.1063 \rightarrow \lambda \simeq 0.15. \quad (3.4)$$

In the above equation, we have inserted the specific geometric data used in our simulations where the only free parameter is  $h/H$ . Specifically, the values are:  $d \simeq 0.182\Delta S$ ,  $\Delta S \simeq 0.13H$  and  $\lambda = 0.14h/H$ . The above estimate matches the numerical value corresponding to the crossing between  $y_{vo}$  and the internal inflection point of Figure 6(a), showing that this simple geometric argument allows the prediction of the threshold value  $h/H$  that defines the establishment of a *dense regime* canopy flow. Note that this value is also the value indicated by Schlichting (1936) to distinguish between the sparse and the dense *k-type* roughness regimes. For values of  $h/H$  exceeding the threshold value, the canopy becomes denser and the depth of the virtual origin saturates towards a value  $\simeq \Delta S$ . Under these conditions, for large values of  $h/\Delta S$ , it is expected that the outer and the internal boundary layers almost decouple with very weak interactions. Finally, in Figure 8, we present three sets of snapshots that provide a qualitative assessment of the conceptual model that has been previously introduced to predict the transition throughout different canopy flow regimes. In particular, Figure 8(a) shows the instantaneous distribution of the streamwise vorticity on a  $y-z$  plane for the four canopy heights. Figure 8(b) and (c) show isovalues of the streamwise and wall-normal velocity fluctuations extracted at the same cross-sectional plane. All the figures clearly show that the canopy acts as a filter for the external flow field allowing the outer flow to penetrate within a depth  $\sim \Delta S$  for the densest cases and  $\sim h$  for the coarsest one. In particular, Figure 8(a) and (b) show how the large logarithmic coherent structures are chopped by the canopy stems and how the increase in canopy height enhances the intensity of the outer flow fluctuations that are progressively less influenced by the constraint of the bottom wall.

### 3.2. Statistical characterisation of the intra-canopy and of the outer flows

To characterise the structure of the regions of the considered canopy flows, we start by considering the mean velocity profiles in semi-logarithmic axes, as shown in Figure 9. The profiles are made dimensionless using two different friction velocities inside and outside the canopy. In particular, for the inner boundary layer, the friction velocity is defined as  $u_{\tau, in} = (\tau_w/\rho)^{1/2}$ , being  $\tau_w$  the skin friction at the bottom wall (i.e.  $y/H = 0$ ). The external profile is normalised with a different velocity scale,  $u_{\tau, out}$ , computed using the total stress evaluated at the virtual origin  $y_{vo}$  as in (3.3).

Figure 9 reveals that, close to the bed, the velocity profiles obtained with different values of  $\lambda$  collapse together only in the viscous sublayer region where, independently of the canopy sparsity, the wall friction dominates over the drag offered by the stems.

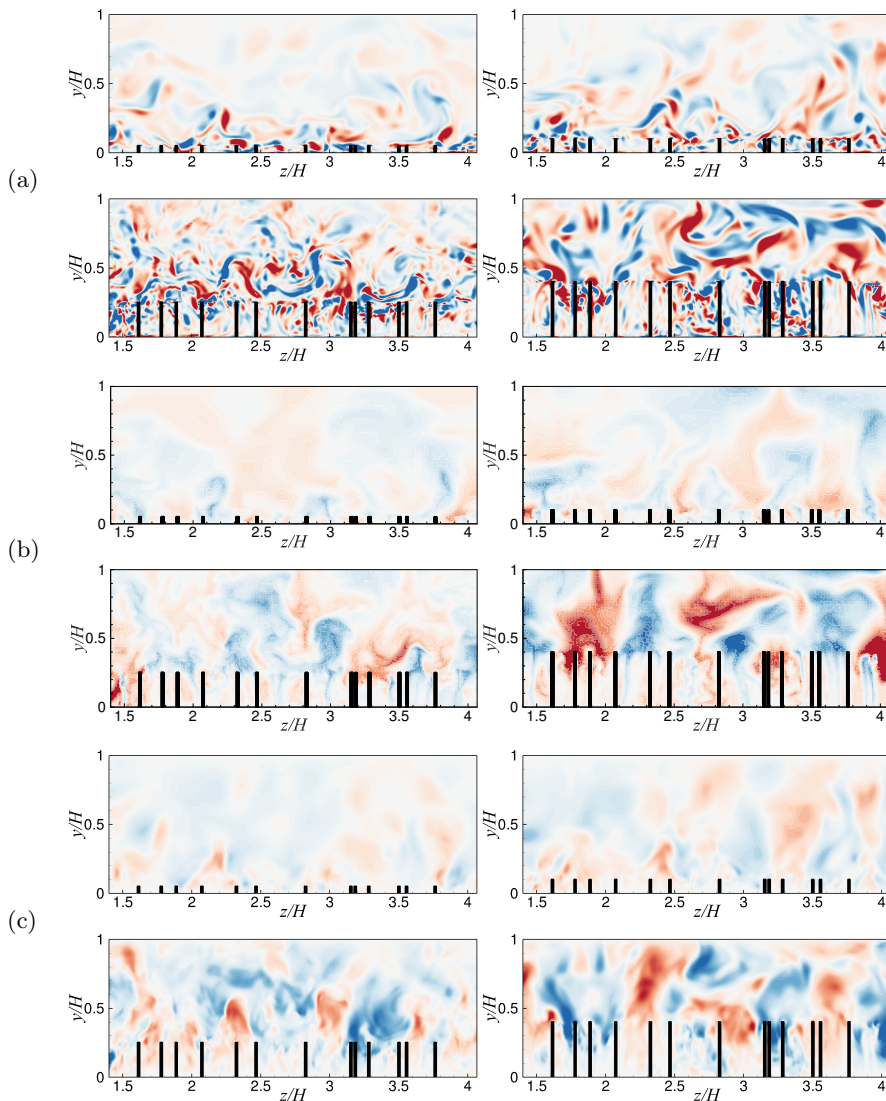


Figure 8: Instantaneous isovalues of the streamwise vorticity fluctuations (a) and of the streamwise (b) and wall normal (c) velocity fluctuations for the four canopy flow configurations. For each sub-figure composed by four panels, the canopy frontal solidity increases clockwise from the left top image (from case *MS*, top left corner to case *DE*, bottom right corner). Data have been extracted from a  $y - z$  cross plane. Red colour is used for positive values while blue is for negative ones. The velocity fluctuations range is  $u'/U_b \in [-0.7, 0.7]$  and  $v'/U_b \in [-0.5, 0.5]$  for all plots. The range of the streamwise vorticity is  $\omega_x H/U_b \in [-10, 10]$ .

Further away from the bed, the shape of the buffer layers is highly affected by the value of  $\lambda$  that determines the importance of the local hydrodynamic effects versus the in-rush of momentum from the outer layer. Unlike the intra-canopy region, the outer flow velocity profiles, scaled with  $u_{\tau,out}$  and with the corresponding viscous length scale  $\delta_\nu = u_{\tau,out}/\nu$ , follow a universal, logarithmic distribution for all  $\lambda$  values. The effect of

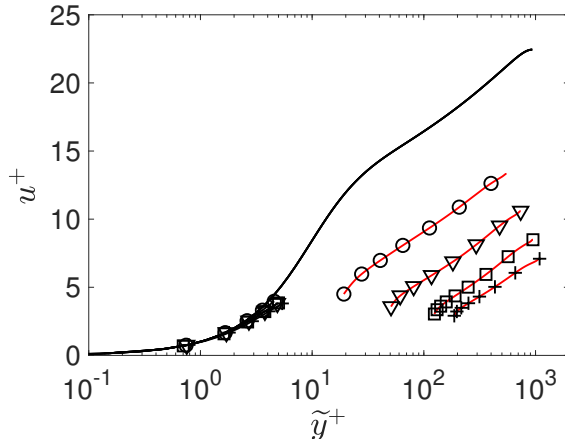


Figure 9: Mean velocity profiles normalised using both the inner wall units (below  $y_{in}^+ \simeq 4$ ) and the outer ones (above  $y_{out}^+ \simeq 10$ , symbols and continuous red lines). The abscissa  $\tilde{y}^+$  represents the wall-normal coordinate rescaled with the inner or outer wall units considering an origin located either on the canopy bed or at the virtual origin  $y_{vo}$ : i.e.  $\tilde{y}^+ = u_{\tau,in}y/\nu$  or  $\tilde{y}^+ = u_{\tau,out}(y - y_{vo})/\nu$ , respectively. The solid black line without symbols refers to the profile of the plane channel flow at  $Re_\tau = 950$  by Hoyas & Jiménez (2008). Symbols as in Table 1. Note that, although the slope of the external velocity profiles is the same, they do not match because the virtual origins are located at different coordinates.

the canopy sparsity is limited to the shift of the logarithmic layer revealing that, seen from the outer flow, the canopy stems can be simply interpreted as roughness elements which height is determined by the value of  $\lambda$ .

Consider the logarithmic law for a turbulent boundary layer over a rough wall, that can be written as

$$U_{out}^+ = \kappa^{-1} \log(y_{out}^+) + 5.5 - \Delta U_{out}^+, \quad (3.5)$$

where  $\Delta U_{out}^+$ , termed *roughness function* (see Hama 1954; Perry *et al.* 1969; Jiménez 2004), is a wall-offset that takes into account the increased friction due to roughness. Figure 10 shows that the roughness function increases monotonically with the value of  $\lambda$  (or, equivalently, with  $h/H$ ), approaching an asymptotic value as the canopies become denser. This behaviour is related with the previously discussed saturation of the location of the virtual origin for increasing  $\lambda$  values that, in turns determines the roughness solidity seen by the outer flow, i.e.  $\lambda_{eff} = d(h - y_{vo})/\Delta S^2$ . Apart from the roughness function  $\Delta U^+$ , the effect of the roughness on the mean flow can be measured by other, interchangeable quantities (Jiménez 2004) such as the effective sand roughness  $k_s$  (Nikuradse 1933) defined via the modified log-law,

$$U_{out}^+ = \kappa^{-1} \log\left(\frac{y-h}{k_s}\right) + 8.5. \quad (3.6)$$

By assuming that the outer turbulent flow sees the canopy as a rough wall, the portion of the canopy that goes from the virtual origin to the canopy tip can be interpreted as a surface covered by cylindrical obstacles characterised by height,

$$k^+ = \frac{k u_{\tau,out}}{\nu} = \frac{(h - y_{vo}) u_{\tau,out}}{\nu}. \quad (3.7)$$

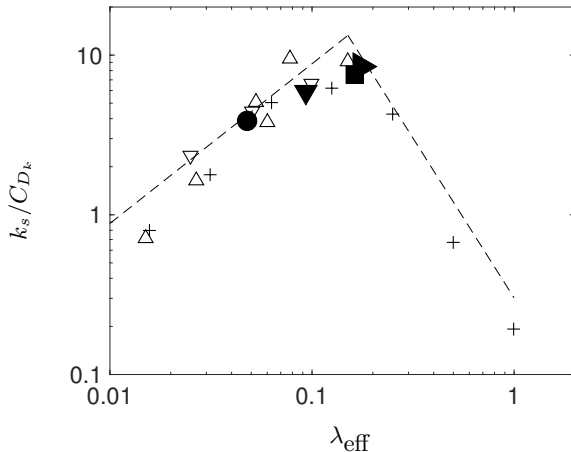


Figure 10: Equivalent sand roughness  $k_s/k$  seen by the outer flows of the canopy versus the effective solidity  $\lambda_{\text{eff}}$ . As in Jiménez (2004, p.179, Figure 1a),  $k_s/k$  has been corrected with the drag coefficients  $C_D$  computed at the stem mid location where the local flow is unaffected by the ends. The dash line represents a theoretical case where  $k_s/k \propto \lambda_{\text{eff}}$ . Open symbols refer to non-circular roughness element:  $\triangle$ , spanwise fences (Schlichting 1936);  $\nabla$ , spanwise fences (Webb *et al.* 1971);  $+$ , spanwise cylinders (Tani 1987). Filled symbols refer present results:  $\bullet$  case *MS*,  $\blacktriangledown$  case *TR*,  $\blacksquare$  case *MD* and  $\blacktriangleright$  case *DE*

All the four considered cases are characterised by a value of  $k^+ \gg 1$ , a situation in which the drag due to the elements dominates on the viscous one. This type of roughness, termed *k-type* (Jiménez 2004), may induce two different flow regimes which inception depends on the relationship between the ratio  $k_s/k$  and the solidity  $\lambda_{\text{eff}}$  (Schlichting 1936). Specifically, for values of  $\lambda_{\text{eff}} \lesssim 0.15$ ,  $k_s/k$  linearly increases with  $\lambda_{\text{eff}}$ . For  $\lambda_{\text{eff}} \gtrsim 0.15$ , the roughness elements start shielding one each other and  $k_s/k$  starts decreasing as  $k_s/k \propto \lambda_{\text{eff}}^{-p}$ , with  $p \in [2, 5]$  (Jiménez 2004).

Figure 10 shows the ratio  $k_s/k$  as a function of  $\lambda_{\text{eff}}$  for the four cases considered in this work. Note that the ratio  $k_s/k$  has been corrected with the drag coefficient value suggested in Figure 1(a) of Jiménez (2004). From Figure 10, it appears that all the considered cases appear to belong to the *sparse-k-type* regime with the values corresponding to  $h/H = 0.25$  and  $h/H = 0.40$  in the range of the *sparse-dense* transition. Also note that, when  $y_{vo}$  saturates,  $h - y_{vo} \simeq h$  and  $\lambda_{\text{eff}} \simeq \lambda$ , thus, although the definition of dense and sparse canopies differs from the one used for the rough surface seen by the outer flow, when approaching the dense regime for the outer flow the separation value between rough regimes can be inferred using indifferently  $\lambda \simeq 0.15$  or  $\lambda_{\text{eff}} \simeq 0.15$ .

Before introducing the Reynolds stresses distributions, we briefly discuss the selection of appropriate velocity and length scales enabling a direct comparison between the four canopy flows. The velocity scale that we have chosen is based on the local value of the total shear stress,

$$u_{\tau,l}(y) = \sqrt{\frac{\mu \, d_y \langle u \rangle - \rho \langle u'v' \rangle}{\rho (1 - y/H)}}. \quad (3.8)$$

This definition, incorporating the effect of the mean drag exerted by the canopy on the flow, allows the dimensionless total stress to vary linearly with the wall-normal distance

(Monti *et al.* 2019). We can associate to the friction velocity (3.8) a local Reynolds number  $Re_{\tau,l}(y) = u_{\tau,l}(y)H/\nu$  based on the total channel height.

The appropriateness of using a local friction velocity as a scaling factor has been previously appraised by other authors for both smooth and manipulated walls (Tuerke & Jiménez 2013; Jiménez 2013; Sharma & García-Mayoral 2018). The well behaved scaling properties of (3.8) are also confirmed by the present results. In particular, Figure 11 shows a comparison between the diagonal Reynolds stresses normalised with the external friction velocity  $u_{\tau,out}$  obtained using the total stress at the virtual origin (3.3) (plots in the left column), as opposed to the ones obtained by normalising with the local friction velocity defined in (3.8) (plots in the right column). The panels on the left column of Figure 11 clearly show that the diagonal Reynolds stresses obtained for different values of  $\lambda$  do not collapse inside the region occupied by the canopy also indicating that the values of the maxima decrease monotonically when increasing  $\lambda$ . This systematic decrease of the stresses peak values is induced by the variations in the mean drag offered by the canopy. When the dimensionless stress values are defined using the velocity scale (3.8), which includes the mean drag contribution to the stresses, the variations in the values of the maxima are largely reduced (as shown in the right panels of Figure 11) leading to an almost total collapse for all components in the sparsest cases. In the two densest cases, the peaks of the streamwise and of the wall-normal components increase, while the spanwise fluctuations show a different behaviour decreasing in the denser cases. Concerning the choice of the length scale, we have considered both an outer and an inner scaling. The former is based on the external length scale (in our case, the depth of the open channel  $H$ ), while the latter employs an inner viscous scale,  $\delta_\nu = \nu/u_\tau$ . The appropriateness of  $H$  as a length scale for the outer flow is clearly visible in Figure 11 that shows a collapse of all the diagonal stresses distributions when moving away from the canopy, independently of the choice of the velocity scale. A more comprehensive comparison of the distribution of the velocity fluctuations away from the region occupied by the canopy is shown in Figure 12, where we have also incorporated the data from the direct numerical simulation of a plain channel flow over smooth walls at  $Re_\tau = 950$  of Hoyas & Jiménez (2008). A good collapse is obtained for all fluctuations in all cases, except in the region  $y/H \simeq 1$  where the comparison between a full channel and an open channel cannot be made. The marginal difference between the Reynolds stresses distributions obtained in a smooth and in rough turbulent channel flow was also highlighted by Scotti (2006), who analysed the flow over a set of transitional, *k-rough* type surfaces.

Concerning the most relevant internal length scale, the choice is between several possibilities since the filamentous layer covering the bed introduces several extra geometrical and physical scales, e.g. the height,  $h$ , and the diameter of the stems,  $d$ , the average separation between them,  $\Delta S$ , the location of the mean velocity profile's inflection points and the location of the virtual origin for the outer flow,  $y_{vo}$ . In an attempt to find a length scale delivering a unified behaviour, we introduce a *scaled viscous unit*,  $y_\alpha^+$ , defined using the localised friction velocity (3.8) corrected with a *stretching* factor  $\alpha$ :

$$y_\alpha^+ = \frac{1}{\alpha} \frac{u_{\tau,l} y}{\nu}. \quad (3.9)$$

The role of  $\alpha$  in the above definition is to adapt the scaling to conditions that depend on the sparsity of the canopy (i.e. on the eventual saturation of length scales that depend on the value of the solidity  $\lambda$ ). Figure 13(a) reveals that in denser canopies the stretching factor should be set to the dimensionless canopy height,  $h/H$ , thus leading

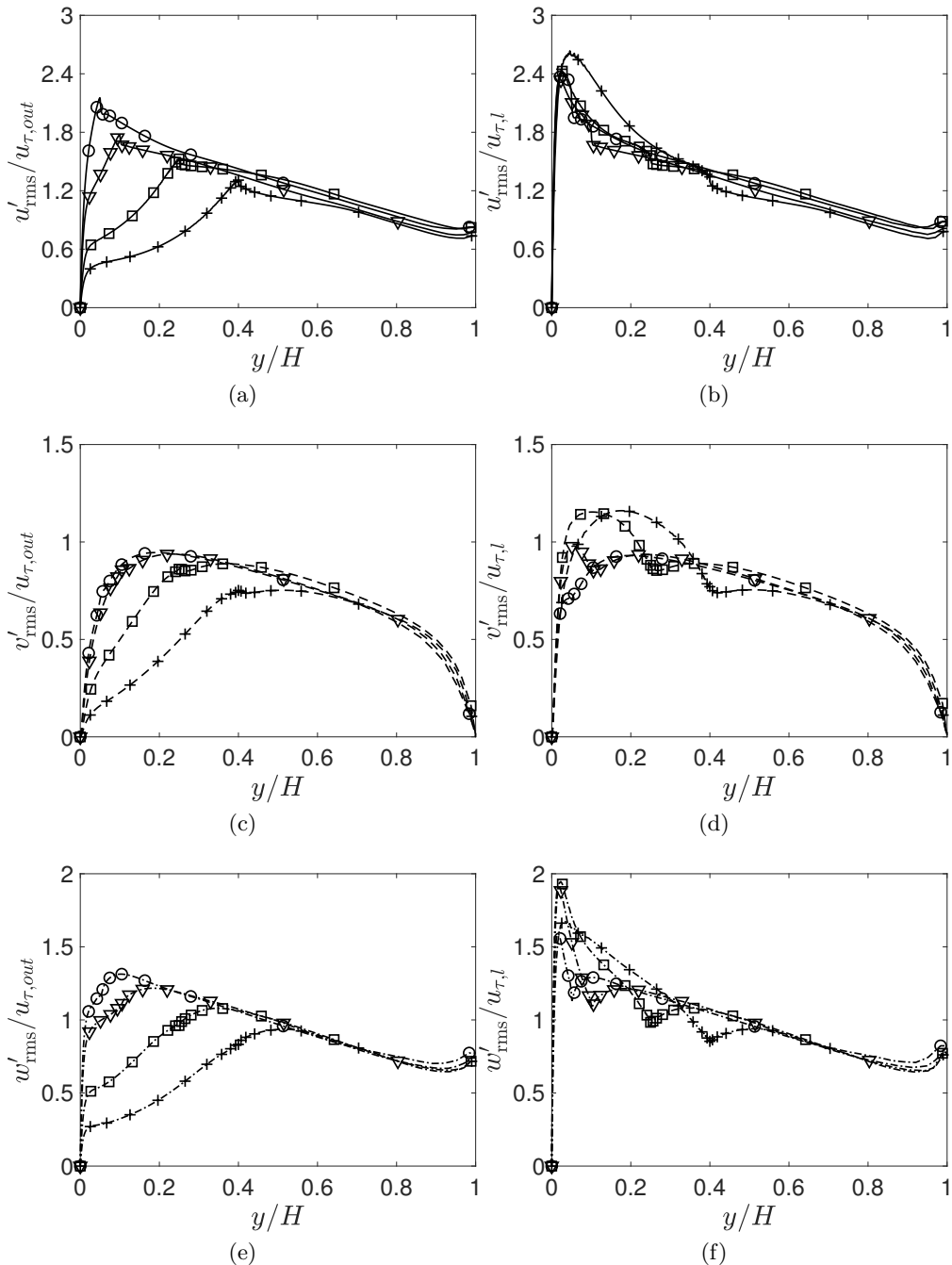


Figure 11: Diagonal Reynolds stresses distributions versus the wall-normal, external coordinate  $y/H$ : panels (a) and (b): streamwise component; panels (c) and (d): wall-normal component; panels (e) and (f): spanwise component. The distributions on the left panels are made non-dimensional with the friction velocity computed at the virtual origin,  $u_{\tau,out}$ , whilst the distributions in the right panels are rescaled with the local friction velocity  $u_{\tau,l}$  (3.8). Symbols as in Table 1; line styles are: —  $u'_{rms}$ ; - - -  $v'_{rms}$  and - · - ·  $w'_{rms}$ .

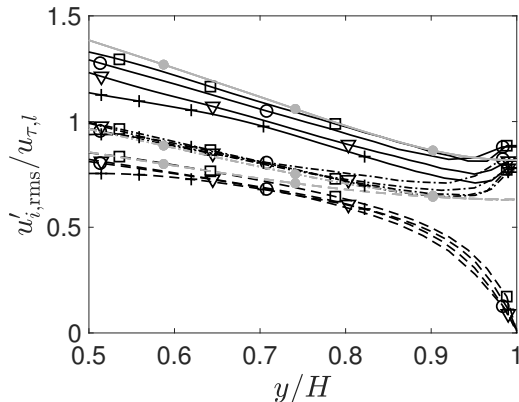


Figure 12: Wall-normal distribution of the diagonal Reynolds stresses in the outer region (i.e. above the canopy) made dimensionless with the local friction velocity  $u_{\tau,l}$ , defined in (3.8), as a function of the wall-normal coordinate  $y/H$ . Line styles as in Figure 11 and open symbols as in Table 1. The grey lines refer to the diagonal Reynolds stresses of a channel flow over a smooth wall at  $Re_{\tau} = 950$  (Hoyas & Jiménez 2008).

to the definition

$$y_h^+ = \frac{u_{\tau,l} y}{\nu} \frac{H}{h} = \frac{y}{h} Re_{\tau,l}. \quad (3.10)$$

Differently, for sparser canopies, e.g. cases *MS* and *TR*, Figure 13(b) suggests that an appropriate value for the stretching factor  $\alpha$  could be the average stem-to-stem spacing  $\Delta S/H$ . With this choice, the dimensionless wall-normal coordinate reads as

$$y_{\Delta S}^+ = \frac{u_{\tau,l} y}{\nu} \frac{H}{\Delta S} = \frac{y}{\Delta S} Re_{\tau,l}. \quad (3.11)$$

Although in this work we did not consider the effects of the variations of the in-plane density (i.e.  $\Delta S$ ), in view of the previously exposed conceptual model and previous works on *k-type* roughness (Leonardi *et al.* 2007), it seems physically sound to assume that it is the ratio  $\Delta S/h$  that sets the size of the eddies that can penetrate the canopy in a sparse canopy flow regime. Finally, Figure 13 shows that the intermediate case *MD*, where  $h/H = 0.25$ , exhibits a consistent profile that is independent of the chosen  $\alpha$  factor, possibly because of the transitional nature of this specific case.

A confirmation of the validity of the proposed scaling is provided in Figure 13(c) where we present the wall-normal distribution of the viscous and Reynolds shear stresses (made dimensionless with  $\rho u_{\tau,l}^2$ ) versus the dimensionless coordinate  $y_{\alpha}^+$  defined in (3.9). Selecting the values of  $\alpha$  defined above as a function of the actual regime, we obtain a good collapse for all the distributions.

The two different length scales that we have defined for the intra-canopy and the outer flow will be used separately in the two regions to determine the non-dimensional wall-normal coordinates. In the particular case of dense canopy regimes (e.g. cases *MD* and *DE*), the separation between the inner and outer regions is not fixed by the tips of the stems but by the location of the virtual origin: the inner region spanning the interval between  $y/H = 0$  and  $y/H \sim y_{vo}/H$  and the outer one between  $y/H \sim y_{vo}/H$  and  $y/H = 1$ . In the neighbourhood of  $y_{vo}$ , the two regions eventually overlap with the separation between regions becoming sharper for increased values of the solidity.

We close the discussion on the mean behaviour of the considered canopy flows by providing a brief, comparative analysis of the root mean square distribution of the

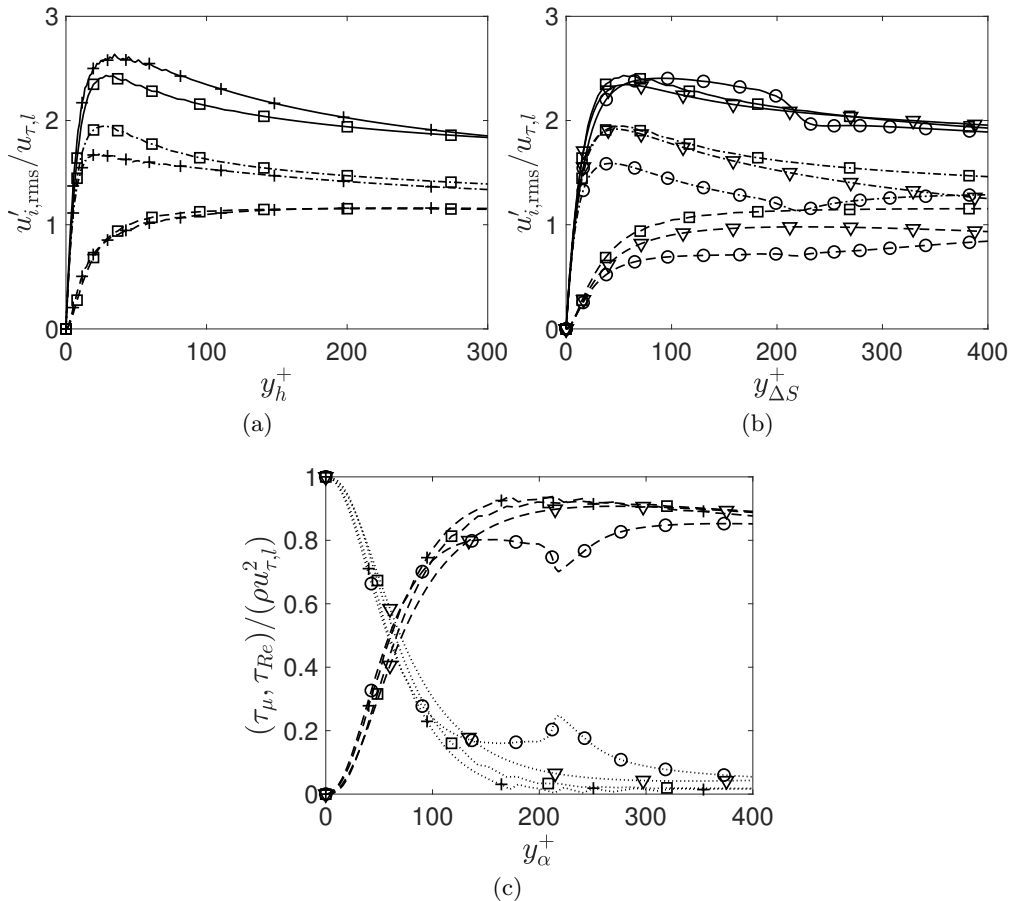


Figure 13: (a) and (b). Wall-normal distributions of the diagonal Reynolds stresses within the intra-canopy region. The stresses are made dimensionless using the local friction velocity  $u_{\tau,l}$ , defined in (3.8). In (a) only the dense cases *MD* and *DE* are represented using as a wall-normal coordinate the non-dimensional variable  $y_h^+$ , defined in (3.10). In (b) the distributions are shown for the sparse cases (*MS* and *TR*) and for the marginally dense case *MD* using as a wall-normal coordinate the dimensionless variable  $y_{\Delta S}^+$  defined in (3.11). (c) Wall-normal distributions of the viscous  $\dots\dots\dots$  and of the Reynolds shear stresses  $-\ - - -$  made dimensionless with the local shear  $\rho u_{\tau,l}^2$ . The wall-normal coordinate corresponds to the non-dimensional variable  $y_\alpha^+$ , as in (3.9), with  $\alpha = h/H$  for the denser cases *MD* and *DE*, and  $\alpha = \Delta S/H$  for the sparser cases *MS* and *TR*. For all panels, symbols as in Table 1 and line-styles as in Figure 11.

velocity fluctuations. Further analysis of the contribution of the flow structures on the genesis of the fluctuations specific to each regime, will be provided in the following subsection. Figure 13 shows the wall-normal distribution of the mean diagonal Reynolds stresses and of the total stresses. The distributions are displayed using two different non-dimensional coordinates in two separate panels: the left panel concerns the dense cases (the non-dimensional  $y$  being the one given in (3.10)), the right one the sparser ones (non-dimensional  $y$  as in (3.9)).

We start by observing that the maxima of the streamwise velocity fluctuations

decrease as the canopy sparsity is increased and that the most sparse case *MS* is characterised by an almost flat distribution within the canopy except in the region close to the bed. This behaviour is consistent with the alternating presence of the stems that locally decelerate the flow driven by the imposed pressure gradient. Clearly, the value of  $\lambda$  determines the intensity of the stems blockage effect that becomes weaker for sparser conditions.

Concerning the wall-normal component of the Reynolds stresses, it is observed that the two denser cases *DE* and *MD* present a distribution that substantially does not differ from the one of a standard, smooth-wall channel flow (see for example Hoyas & Jiménez 2008). This behaviour is easily understood by noticing that denser canopies can be regarded as porous media with a high wall-normal permeability that does not hinder sweeps and ejections from and towards the outer flow to take place in a medium bounded by a *distant*, impermeable bed. The sparser cases show a different behaviour with the wall-normal velocity fluctuations decreasing when the solidity is decreased and the impermeability condition becoming more influential on the outer flow structure.

Finally, the spanwise velocity fluctuations show a behaviour that does not follow the variations of  $\lambda$  monotonically. In particular, we notice an overall increase in  $\langle w'w' \rangle$  when moving from the *DE* to the *MD* case, an almost unchanged distribution for the transitional cases *MD* and *TR*, and a final decrease in the *MS* case. The increase in the spanwise velocity fluctuations observed in the transitional cases, *MD* and *TR*, has been explained by Monti *et al.* (2019) in terms of spanwise deviations of the intra-canopy flow that preferentially penetrates the layer through wall-normal sweeps and ejections generated by the dynamics of the outer, logarithmic layer structures. The complete interpretation of the wall-normal distribution of the velocity fluctuations will be presented in the following sub-section.

### 3.3. The structures of the canopy flows

Further insight on the emergence and on the organisation of the large coherent structures that characterise the various flow regimes when different solidities are considered can be obtained by looking at the spectral energy content of the fluctuations of the velocity components.

We start by considering Figure 14 that shows the magnitude of the one-dimensional premultiplied cospectra of the Reynolds shear stress,  $|\kappa_x \Phi_{u'v'} / u_{\tau,l}^2|$  (or  $|\kappa_z \Phi_{u'v'} / u_{\tau,l}^2|$ , where  $u_{\tau,l}(y)$  is the local friction velocity defined in (3.8)), as a function of the distance from the bed and of the streamwise (top row) and the spanwise (bottom row) wavelengths. Each row incorporates four panels corresponding to the cospectra that have been obtained using the four considered  $\lambda$  values. In this figure and in the premultiplied spectra of the velocity fluctuations (to be presented later), the wavelengths and wall-normal distances have been made dimensionless with the open-channel height,  $H$ . Both the cospectra and premultiplied spectra have been plotted using *log-log* axes to facilitate the interpretation of the results within the intra-canopy region.

Observing the cospectra of Figure 14 obtained for different solidities, we notice that all of them present at least two distinct peaks whose locations move towards the  $y$  coordinates of the two inflection points of the mean velocity profile (yellow and red horizontal, dashed lines in every subfigure) as  $\lambda$  is increased. More precisely, the outer peak approaches asymptotically the tip of the canopy for increasingly dense conditions with the associated streamwise and spanwise wavelengths of sizes  $O(H)$ . Since  $\langle u'v' \rangle$  is a good indicator of spanwise-oriented coherent structures, the outer peak suggests the presence of a set of rollers centred at the canopy tip. Their presence is confirmed by visual inspection of the streamlines plotted on the  $x$ - $y$  side of the computational boxes

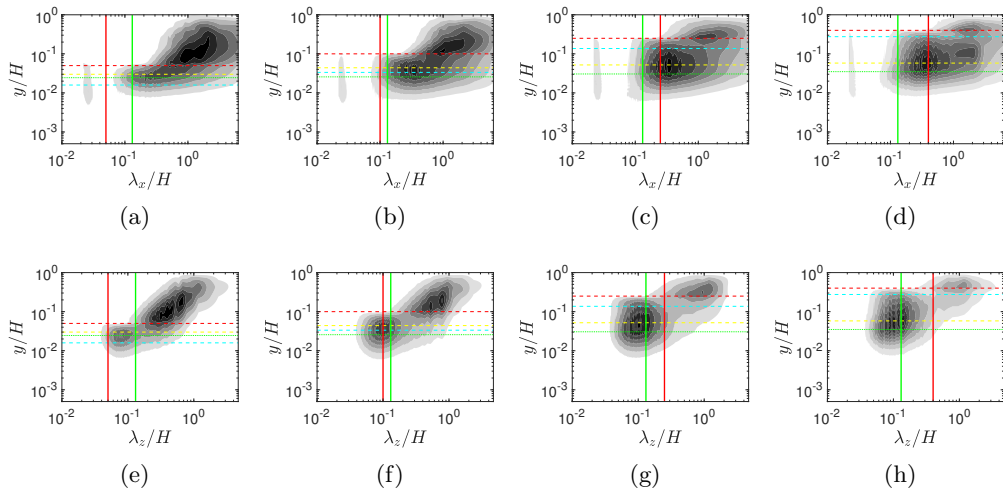


Figure 14: Magnitude of the premultiplied cospectra of the streamwise and spanwise velocity fluctuations  $u'$  and  $v'$  as a function of the wall-normal coordinates in outer units. Panels (a) to (d) refer to the dependence from the streamwise wavelengths (in outer units) for increasing values of  $\lambda$  (i.e.,  $\lambda = 0.07, 0.14, 0.35$  and  $0.56$ ); contour levels range in the interval  $[0, 0.4]$  with an increment of  $0.02$ . Panels (e) to (h) refer to the spanwise wavelengths for the same increasing set of  $\lambda$  values; contours extracted in the  $[0, 0.5]$  range with an increment of  $0.05$ . Vertical solid lines: red is  $h/H$ , green is  $\Delta S/H$ . Horizontal dashed lines: yellow is the location of the inner inflection point, red is the the canopy height (outer inflection point), cyan is the location of the virtual origin; the green dotted line is the location of maximum curvature of the mean velocity profile.

of the four considered cases in Figure 15 (streamlines obtained by spanwise averaging an instantaneous realisation of the  $u'$  and  $v'$  velocity components).

The appearance of spanwise oriented rollers is a ubiquitous feature of many flow fields over textured surfaces that induce an inflection point in the mean velocity profile, e.g. flow over canopies, see Nepf (2012) or Finnigan *et al.* (2009), or porous and ribbleted walls, see Jiménez *et al.* (2001) and García-Mayoral & Jiménez (2011). In our case, the outer inflection point is generated by the discontinuous drag imposed by the canopy on the mean flow at its tip. As observed by other authors, the resulting scenario resembles the one of a plane mixing layer (Raupach *et al.* 1996; Finnigan 2000; Nepf 2012) sharing with it also the appearance of a system of spanwise rollers that form as a consequence of a Kelvin-Helmholtz-like instability. The streamwise wavelength  $\Lambda_x$  associated with these rollers in dense canopy flows (i.e.  $\lambda \gg 0.1$ ) has been found to be within the range  $7 < \Lambda_x/L_s < 10$  (Raupach *et al.* 1996), where  $L_s$  is a measure of the vorticity thickness above the canopy tip,

$$L_s = \frac{\langle u \rangle_{tip}}{\partial_y \langle u \rangle_{tip}} = \frac{1}{2} \delta_\omega. \quad (3.12)$$

Raupach *et al.* (1996), after analysing data from several experiments on dense canopy flows, provided a sharper estimate as  $\Lambda_x = 8.1L_s$ . In Figure 16, we compare this last estimate of  $\Lambda_x$  with the one computed in our canopy flows associated with the outer peaks of Figure 14, as a function of the shear length,  $L_s$ . Clearly, the estimate provided by Raupach *et al.* (1996) holds only for the two denser scenarios while for the two

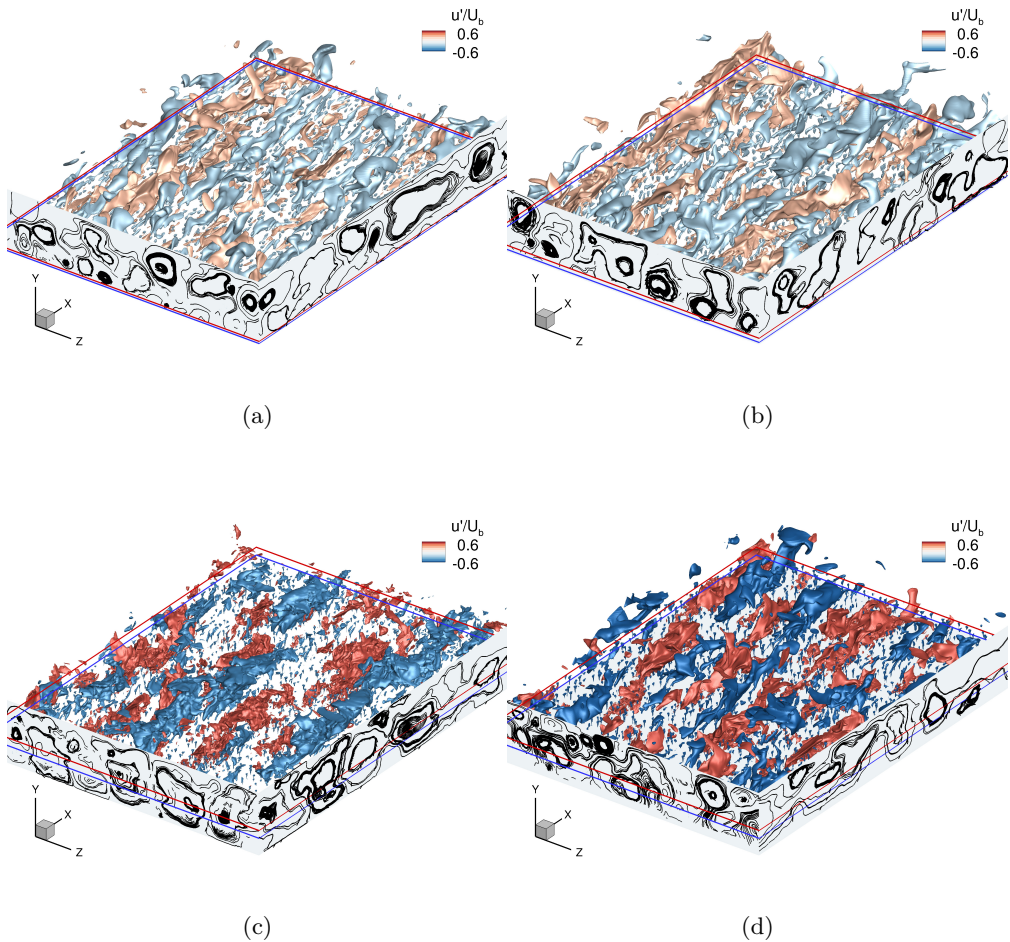


Figure 15: Instantaneous isosurfaces of streamwise velocity fluctuations. The streamlines drawn on the lateral sides have been obtained by averaging the instantaneous velocity fluctuations along the normal to the considered faces: the spanwise direction ( $\langle u \rangle_z$ ,  $\langle v \rangle_z$ ) for the left lateral side and the streamwise direction ( $\langle v \rangle_x$ ,  $\langle w \rangle_x$ ) for the frontal face. (a), (b), (c) and (d) correspond to the cases *MS*, *TR*, *MD* and *DE* respectively. The plane indicated with the red lines corresponds to the tip of the canopy, while the blue line indicates the plane at a distance  $y_{vo}$  from the bed.

sparser canopies *MS* and *TR* the correlation is not verified showing a linear relation  $\Lambda_x = 19.5L_s - 4$  instead. A possible explanation for this inconsistency can be attributed to the fact that the mean velocity in the inner canopy region can no more be neglected and that (3.12) is no more a valid estimate of the vorticity thickness above the canopy.

Concerning the inner peak of the  $\langle u'v' \rangle$  cospectra, it is noticed that its wall-normal location matches the position of the inner inflection point for all the considered  $\lambda$  values and that for increasing values of the canopy solidity, the interior maxima correspond to modes with  $\lambda_x/H \simeq h/H$  and  $\lambda_z/H \simeq \Delta S/H$ . From Figure 17, showing the mean velocity profile inside the canopy, it is also noticed that Fjørtoft's criterion (i.e. a necessary

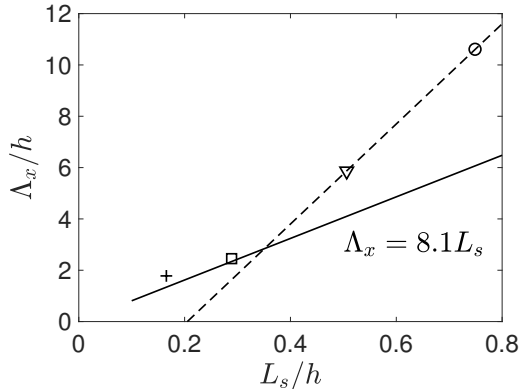


Figure 16: Streamwise wavelength  $\Lambda_x$  of the large coherent motions triggered by the KH-like instability versus the shear length  $L_s$ . The solid line represents  $\Lambda_x = 8.1L_s$  (Raupach *et al.* 1996), whilst the dashed line represents  $\Lambda_x = 19.5L_s - 4$ . Symbols as in Table 1.

condition for an inviscid flow instability, see Drazin & Reid 1981), given by

$$\partial_{yy}\langle u \rangle(y) [\langle u \rangle(y) - \langle u \rangle(y_s)] < 0, \quad (3.13)$$

for all  $y$  in the neighbourhood of the inflection point  $y_s$ , is satisfied at the interior inflection point (see panel (b) of Figure 17) of the mean velocity profile. This observation leads to the conjecture that the inner peak in the cospectra of  $\langle u'v' \rangle$  may be responsible for the emergence of another, internal shear instability inside the canopy. A series of snapshots offering a visual indication on the structure of the velocity field inside the canopy is provided in Figure 18. Although these snapshots only offer isovalues of the velocity components at selected sets of  $x - z$  planes for case *DE*, it clearly appears that the velocity fluctuations at the location of the inner inflection point (panels (a) to (c)) do not seem to inherit the same organised pattern that characterises planes that are further away from the bottom wall (panels (j) to (l)). This variation of the structure of the velocity field along the normal direction inside the canopy, becomes quite evident when considering the streamwise component of the fluctuating velocity. In particular, on the  $x - z$  plane corresponding to the inner inflection point location, i.e. panel (a), a set of spanwise-oriented wave-like shape emerges with a pattern that appears to be totally uncorrelated with the streamwise-oriented streaks characterising the outer region shown in panel (j). Differently, the pattern that can be observed in panel (a), reminiscent of a KH-like instability with a streamwise modulation, seems to correlate with the structure of the wall-normal velocity in the plane corresponding with the location of the virtual origin shown in panel (e). In the latter, the wall-normal ejections and sweeps are clearly visible in panel (e). The wall-normal fluctuations pervade all the canopy because of the high wall-normal permeability, however, panel (b) shows that they cannot reach the region close to the wall because of the impermeability condition. Here, the solenoidal condition on the velocity field deviates the  $v'$  fluctuations generating modulations of the fluctuations of the other two velocity components (see panels (a), (c), (d) and (f)). In particular, we notice that each strong sweep in panel (e) corresponds to a strong divergence of  $w'$  in panel (c). The meandering behaviour of  $u'$  and  $w'$  on finer length scales is observable in all the panels extracted within the canopy and can be attributed to the presence of the stems. At the edge of the canopy, the short-wavelength fluctuations are still visible, but now the large scale fluctuations are directly inherited from the outer flow structures, i.e. long elongated streamwise velocity streaks and quasi streamwise vortices leave their

footprint in the elongated contours of  $u'$  (see panels (g) and (j)) and in the contours of  $v'$  (panels (h) and (k)) and  $w'$  (panels (j) and (l)). Before looking in details at the structure of the fluctuating velocity fields, following earlier studies (Raupach & Shaw 1982; Nikora *et al.* 2007; Ben Meftah & Mossa 2013; Ben Meftah *et al.* 2014), we consider the field resulting from the time average only. In principle, this average allows us to highlight the presence of the wake behind the elements that contribute to the budget of the kinetic energy especially in the case of coarse canopies, where the dispersive stresses induced by the presence of the stems, become comparable to the Reynolds stresses (Yuan & Piomelli 2014). In the present case, the random distribution of the stems on each tile makes it very difficult to determine the structure of the time averaged field. An attempt to reconstruct a hypothetical field behind a single filament can be done by considering a time-average coupled with a tailored ensemble average over the tiles. The procedure that we have envisaged proceeds in three stages. Firstly, we obtain a time-averaged field over the whole canopy. This mean field is not particularly meaningful as it contains local behaviours inherited from the random distribution of the filaments over the tiles. To remove this effect, in a second stage, we consider a virtual cuboid with a  $2\Delta S \times 2\Delta S$  base and a height  $h$ . All the velocity fields over each tile volume are then translated in such a way that the location of their respective stems matches the centre of the cuboid base. The resulting, translated fields that will fill the cuboid are then ensemble-averaged to produce an intermediate mean field. Finally, to obtain the double averaged field over a  $\Delta S \times \Delta S$  tile, analogous to the one that would correspond to a uniform filaments distribution, we average on the cuboid over the  $x$  and  $z$  direction exploiting the periodicity and the parity of the averaged velocity field. The double averaged fields obtained through this procedure for the four canopy configurations are shown in Figure 19. Panel (a) of the figure shows that in the *MS* case the wall-normal velocity, close to the canopy tip, presents sweeps on both the frontal and the lee side of the stem. However, when moving deeper in the canopy the mean wall-normal velocity becomes negative at the leading edge and positive at the rear producing a strong mean deflection of the streamlines around the filaments in the region close to the bottom wall. A similar, although smoother scenario can also be appreciated in panel (b) for the *TR* case. For the denser cases, *MD* and *DE*, panels (c) and (d) show a different distribution of the averaged field with the wall-normal velocity having a mean sweep and ejection on both the lee and wind side of the stems independently of the distance from the canopy edge. Also, the streamlines in the horizontal planes appear to be much smoother and representative of a typical flow around a two-dimensional cylinder.

To shed further light on the structure of the fluctuating velocity fields obtained when different solidity values are considered, we turn our attention to the premultiplied spectra of the velocity fluctuations. In Figure 20 we present the spectra associated with the fluctuations of the three velocity components as a function of the streamwise wavelength and the distance from the bed. Figure 21 shows the spectra as a function of the spanwise wavelength instead. These two figures are organised as a  $4 \times 3$  matrix of panels in which each panel  $(i, j)$  represents the spectra of the fluctuations associated to the  $j^{\text{th}}$  velocity component and the  $i^{\text{th}}$  solidity value (i.e.  $\lambda_{i=1, \dots, 4} = [0.07, 0.14, 0.35, 0.56]$ ).

All the spectra of Figures 20 and 21 share the presence of a peak located outside the canopy. In particular, the streamwise velocity fluctuations show a clear external peak above the canopy tip characterised by a very long streamwise wavelength associated with a large scale modulation in the spanwise direction. These outer, large scale, streamwise velocity structures take on the shape of elongated velocity streaks typical of the logarithmic region of wall-bounded flows (Jiménez 2018). The  $u'$  premultiplied spectra, obtained for different  $\lambda$  values, clearly indicate that the coherence length of these streaks scales

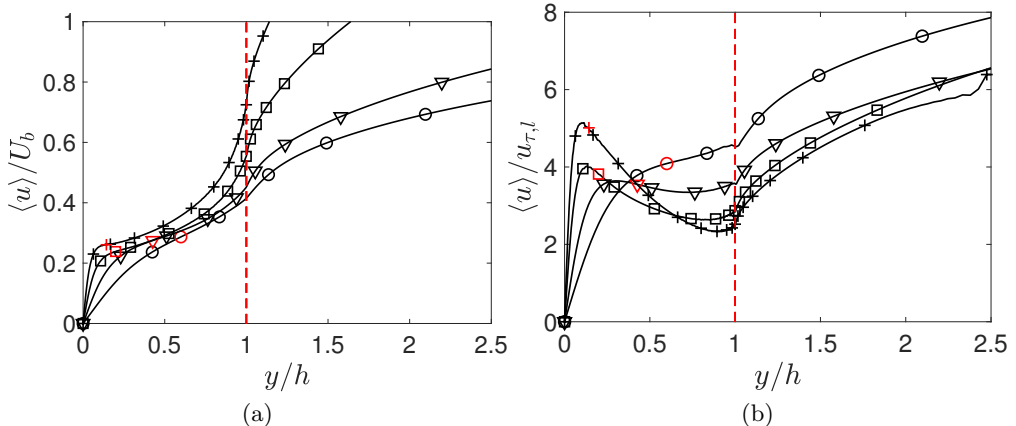


Figure 17: Mean velocity profiles for the four cases normalised with the bulk velocity in panel (a) and the local friction velocity in panel (b), as functions of the distance from the wall normalised with the canopy height  $h$ . The red markers indicate the locations of the inflection point closer to the solid wall, while the red dashed line indicates the location of the canopy edge. Symbols as in Table 1.

in outer units. The presence of these large velocity streaks is also visually confirmed by the streamwise isosurfaces of the snapshots of Figure 15. By looking at the  $y$ - $z$  sides of the computational boxes of the snapshots of the four considered cases in Figure 15 (streamlines obtained by streamwise averaging an instantaneous realisation of the  $v'$  and  $w'$  velocity components), we notice that the outer streamwise velocity streaks are flanked by a set of large streamwise vortices that occupy all the wall-normal portion of the flow outside the canopy. The presence of these streamwise oriented vortices is confirmed by the outer peaks of the premultiplied peaks of  $v'$  and  $w'$  in Figures 20 and 21. We next consider the spectra within the canopy region, starting from the densest case *DE* for which the last rows of Figures 20 and 21 show the presence of two distinct, interior peaks in the energy content of the three velocity fluctuations components. The leftmost peaks in the spectra of  $u'$  and  $w'$  (panels (j) and (l) of Figure 21) are associated with a spanwise length  $\lambda_z \simeq \Delta S$  and are therefore related with the internal meandering motion imposed by the presence of the stems (also visible by the fine spanwise textures of the velocity isocontours (a-d) and (c-f) of the planar snapshots of Figure 18). The leftmost peaks of  $u'$  and  $w'$  in the bottom row of Figure 21 show that the associated streamwise wavelength takes on a value between  $h$  and  $\Delta S$  which is probably related to the coherence length of the wakes formed around the stems.

For sparser conditions, the leftmost peak of  $u'$  and  $w'$  is still observable in Figure 21 (i.e. spanwise structures) just below the location of maximum curvature of the mean velocity profile. Differently, Figure 20 (i.e. streamwise structures) shows a trend of the leftmost peak in merging with the rightmost peak when the value of  $\lambda$  is decreased. It is also noticed that the leftmost peaks associated with the  $v'$  fluctuations in Figures 20 and 21 are located in the same locations as the ones of the cospectra of  $\langle u'v' \rangle$  shown in Figure 14.

The rightmost peaks inside the canopy of the premultiplied spectra of  $u'$  and  $w'$  are associated with larger space scales and thus generated by a different physical mechanism. As briefly mentioned before, when focusing on the dense case *DE* (panels (j) and (l) of

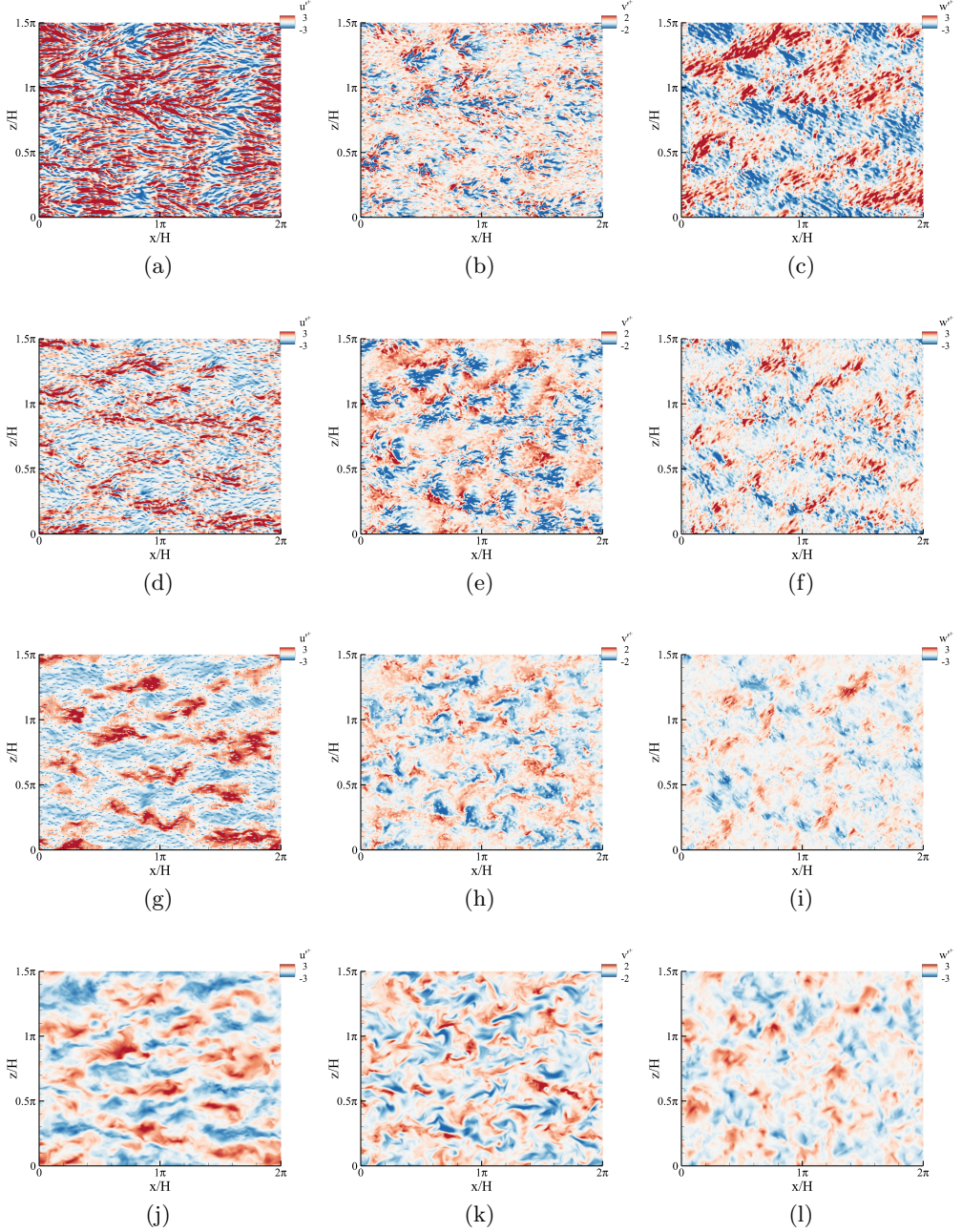


Figure 18: Case *DE*. Instantaneous contours of velocity fluctuations on planes parallel to the wall. Panels (a), (d), (g) and (j): red  $u'/u_{\tau,l} = 3$ , blue  $u'/u_{\tau,l} = -3$ ; Panels (b), (e), (h) and (k): red  $v'/u_{\tau,l} = 2$ , blue  $v'/u_{\tau,l} = -2$ ; Panels (c), (f), (i) and (l): red  $w'/u_{\tau,l} = 3$ , blue  $w'/u_{\tau,l} = -3$ . The planes are located at:  $y/H = 0.059$  (location of the lower inflection point), first row;  $y/H = 0.275$  (location of the virtual origin), second row;  $y/H = 0.40$  (location of the upper inflection point, i.e. the canopy edge), third row;  $y/H = 0.50$  (outer region), fourth row.

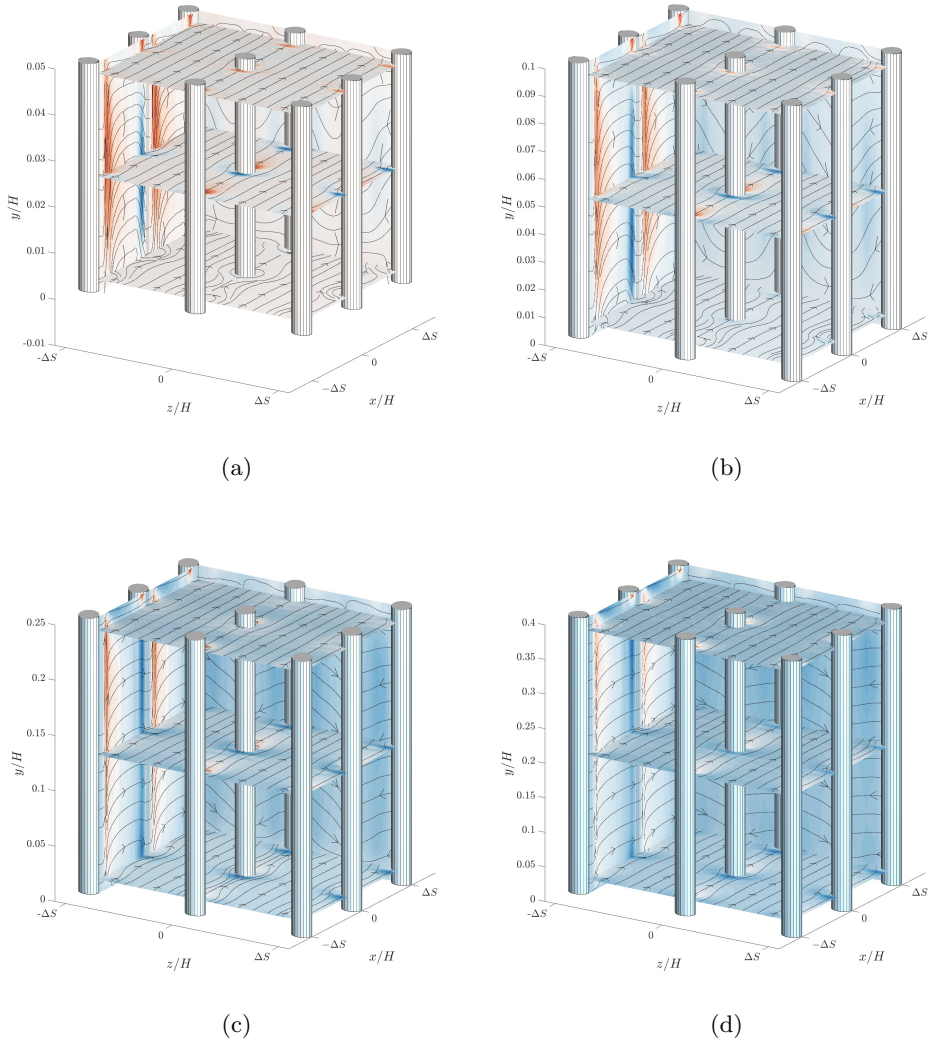


Figure 19: Time and tile averaged flow fields (see text for details on the averaging procedure) corresponding to the four frontal ratios. The first row corresponds to the coarse (a) and semi-coarse case (b) (i.e. *MS* and *TR*); the second row to the semi-dense (c) and dense case (d) (i.e. *MD* and *DE*). In the figures the volume over which the average has been carried out, is repeated by half of its size in the positive and negative  $x$  and  $z$  directions exploiting the periodic conditions. The isocontours on the cross planes correspond to the time and ensemble averaged  $y$  velocity component. Blue are negative values (i.e. mean sweeps), red are positive (i.e. mean ejections). Contours extracted in the range  $[-0.015, 0.027] U_b$ . The horizontal planes are extracted at 5%, 50% and 95% of the canopy height. On these planes, the oriented lines correspond to the three-dimensional streamlines of the double averaged velocity field.

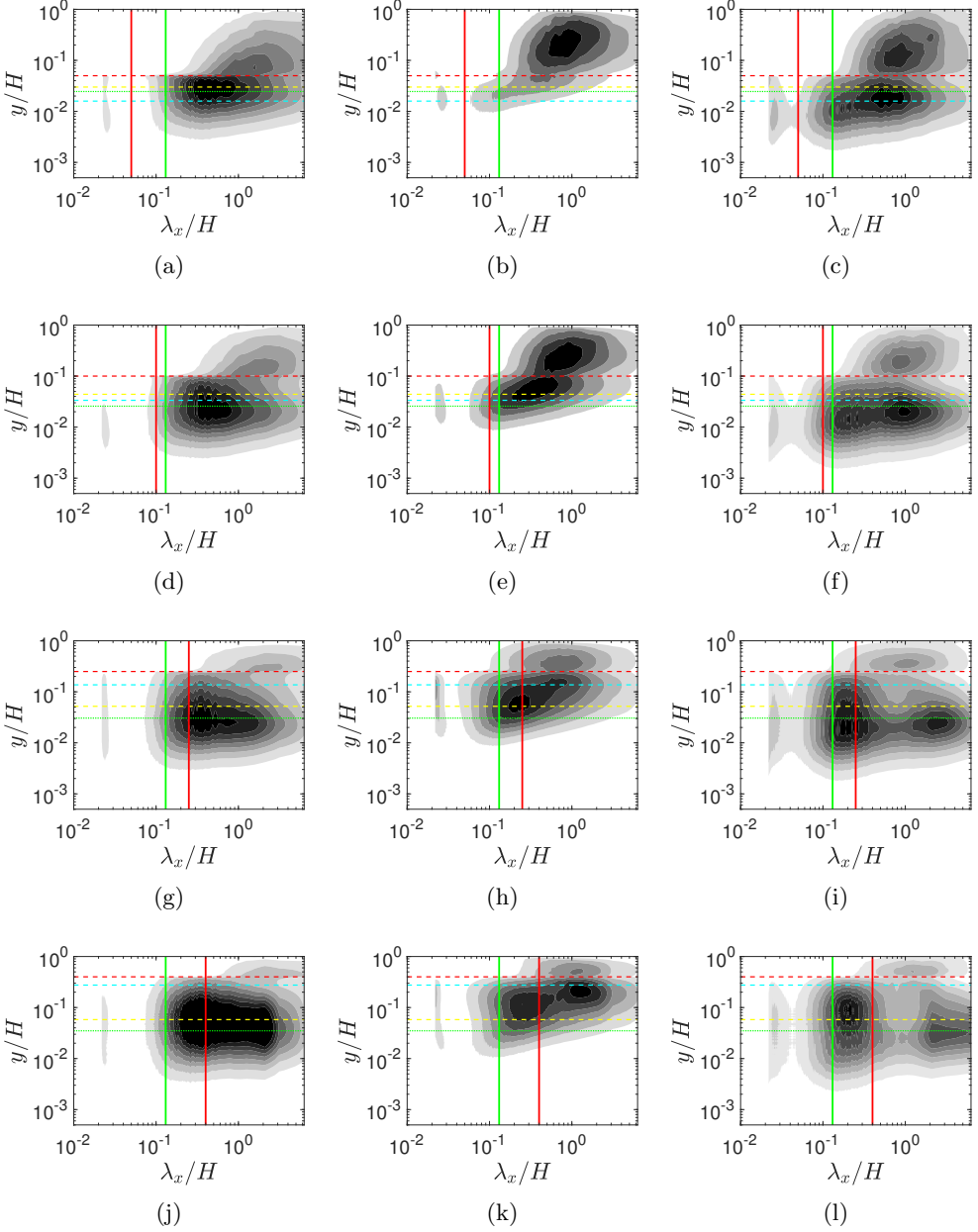


Figure 20: Premultiplied spectra of the velocity components as a function of the streamwise wavelength and the wall-normal coordinates in wall units. Panels (a), (d), (g) and (j):  $\kappa_x \Phi_{w'w'}/u_{\tau,l}^2$  with grey levels range in  $[0, 0.8]$  with a 0.1 increment; Panels (b), (e), (h) and (k):  $\kappa_x \Phi_{v'v'}/u_{\tau,l}^2$  with grey levels range in  $[0, 0.3]$  with a 0.03 increment; Panels (c), (f), (i) and (l):  $\kappa_x \Phi_{w'w'}/u_{\tau,l}^2$  with grey levels range in  $[0, 0.5]$  with a 0.05 increment. The first row (panels a, b and c) refers to the *MS* case; the second row (panels d, e, and f) refers to the *TR* case; the third row (panels g, h, and i) refers to the *MD* case; the fourth row (panels j, k, and l) refers to the *DE* case. Colour lines have the same meaning as in Figure 14.

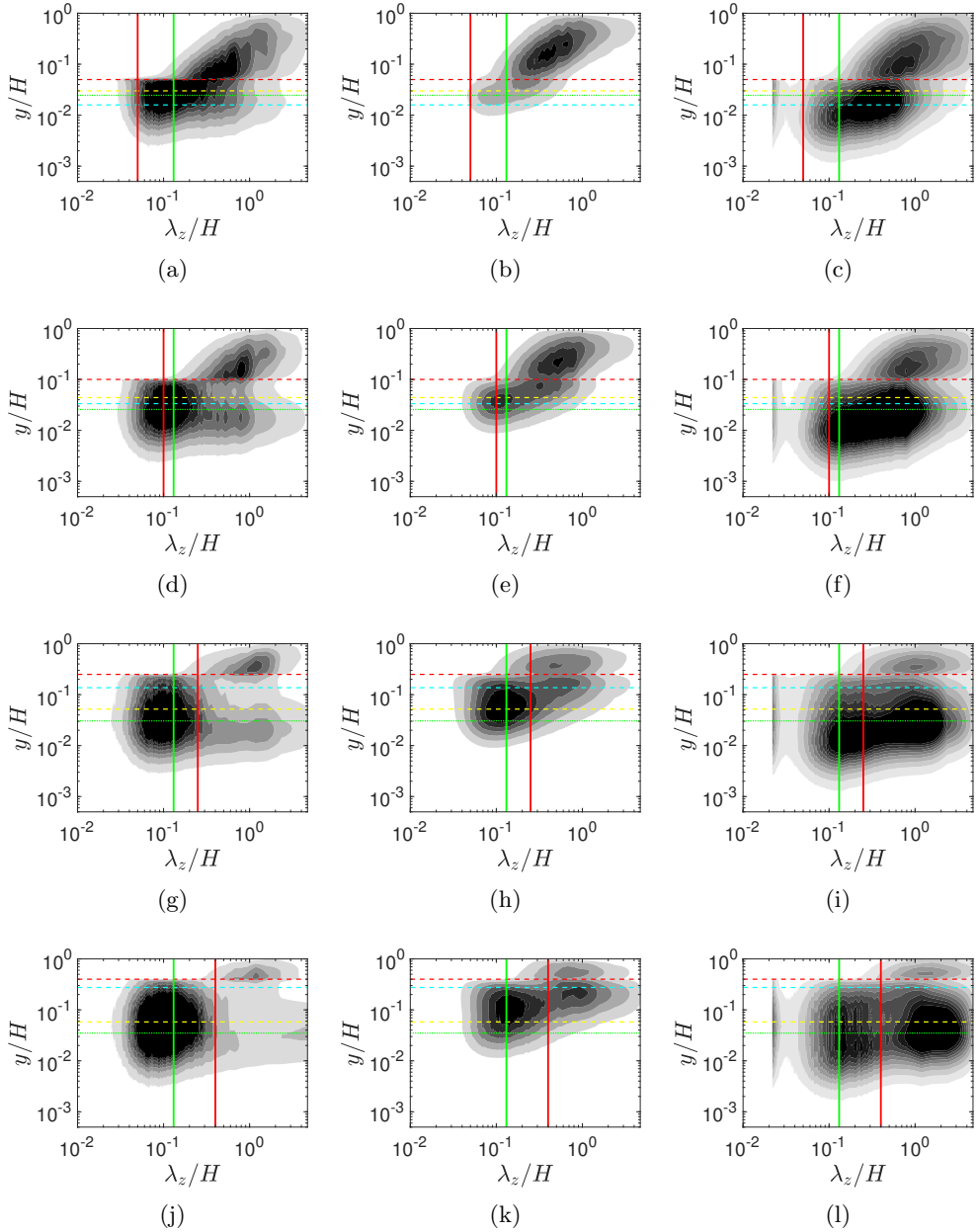


Figure 21: Premultiplied spectra of the velocity components as a function of the spanwise wavelength and the wall-normal coordinates in wall units. Panels (a), (d), (g) and (j):  $\kappa_z \Phi_{u'w'}/u_{\tau,l}^2$  with grey levels range in  $[0, 1.05]$  with a 0.15 increment; Panels (b), (e), (h) and (k):  $\kappa_z \Phi_{v'v'}/u_{\tau,l}^2$  with grey levels range in  $[0, 0.3]$  with a 0.05 increment; Panels (c), (f), (i) and (l):  $\kappa_z \Phi_{w'w'}/u_{\tau,l}^2$  with grey levels range in  $[0, 0.5]$  with a 0.05 increment. Rows ordering, as in Figure 20 and colour lines have the same meaning as in Figure 14.

both premultiplied spectra of  $u'$  and  $w'$ ) and looking at panels (a) and (c) of Figure 18, we realise that a new set of structures is introduced, with the  $u'$  and  $w'$  fluctuations organised in stripes that are highly coherent in the spanwise direction in the  $u'$  case and along a diagonal direction for the  $w'$  case. This organization explains why the spectra of  $u'$  do not have a clear second peak in panel (j) of Figure 21 while  $w'$  does in panel (l) of the same figure. Considering again Figure 18 and comparing panels (a) and (c) (corresponding to planes located by the wall-normal position of the rightmost peak in the spectra of  $u'$  and  $w'$ ) with panels extracted further away from the wall, it becomes quite evident that the flow structure is very different. This observation leads to the conclusion that the region close to the bed is almost decoupled from the regions of the canopy closer to its tip, at least in the denser cases.

The spectra of Figure 21 show that the rightmost peaks of  $u'$  and  $w'$  share the same wavelengths as the rightmost peak of  $v'$  (in the outer flow, or by the canopy tip) although located at different distances from the wall. This correlation is also visually evident from the snapshots of Figure 15 showing a large penetration of the outer quasi-streamwise vortices into the canopy in the wall-normal direction. Since the canopy acts as a porous medium with a  $y$  permeability much larger than the in-plane  $x - z$  ones, the flow that reaches the bottom wall must deflect its momentum to preserve the wall impermeability and the solenoidal condition thereby generating new scales for the  $u'$  and  $w'$  components.

All the aforementioned structures, i.e. the ones triggered by the two inflection points as well as the ones driven by the outer coherent large scale motions mostly interact along the wall-normal direction due to the high  $y$  permeability of the canopy (compared to the  $x - z$ , in-plane permeability components). The high wall-normal permeability also sets the location of the interior inflection point in a situation that resembles the one of a set of planar jets of average cross-section  $\Delta S - d$  striking normally into the bed (Banyassady & Piomelli 2015).

#### 4. Conclusions

In this article, we have considered detailed numerical simulations of rigid, fully submerged canopy flows in different nominal regimes. The nature of the actual fluid mechanic regime in a fully submerged canopy flow is mainly controlled by two geometric quantities: the ratios  $d/h$  and  $h/\Delta S$ . The first one takes into account the slenderness of the stems (i.e. ratio between the diameter and the height), the second measures the ratio between the elements height and their average spacing. When the ratio  $d/h$  is small, it is possible to use only the frontal solidity  $\lambda = (d h)/\Delta S^2$  to determine the onset of a particular canopy flow regime (Nepf 2012). In this work, the solidity  $\lambda$  has been modified only by changing the ratio  $h/\Delta S$  which, for very slender elements in a fully submerged canopy, is the only non-dimensional group built with the geometrical values that characterise the canopy that matters. To our knowledge, this is the first time that resolved simulations are used to explore the nature of different canopy flow regimes and ways to infer a priori their onset. In particular, the most salient outcomes of this research have been: *i*) a detailed characterisation of the *coarse* and *dense* regimes obtained through the analysis of the spectral structure of the velocity fields of the turbulent flows arising inside and outside the canopy; *ii*) a description of the interaction between internal and external flows and how it changes when varying the frontal solidity; *iii*) a proposal for extended and generalised scaling laws covering all submerged canopy flows regimes; *iv*) the identification of a criterion to establish when transition through different regimes takes place that only relies on the shape of the mean velocity profile: the virtual origin of the external flow and the two inflection points; *v*) the recognition of the importance of the most internal

inflection point that can potentially bring in another inflectional instability. Of course, the obtained results must be taken with precaution as we have considered the effect of varying only one non-dimensional parameter and their generalisation needs further exploration that includes the effect of the planar solidity as well.

The basic mechanism responsible for the different behaviours arising in different regimes is the selection process by which the canopy geometry discriminates the structure of the outer flow structures that can penetrate in the filamentous layer. This selection process determines the coordinate of the *virtual* wall seen by the external turbulent shear flow. If  $h > \Delta S$ , the virtual wall is located at  $y \simeq \Delta S$ , while if  $\Delta S > h$  then the location of the virtual origin is a function of the canopy height  $h$  only. Clearly, a transitional condition takes place when  $\Delta S \simeq h$ . We have shown that when this matching condition occurs the frontal solidity takes on the value  $\lambda \simeq 0.15$ . This value is commonly accepted as the one that separates dense from sparse regimes in canopy flows (Nepf 2012) and turbulent flows over  $k$ -type roughness (Schlichting 1936). Our simulations have also proved that in this condition the location of the virtual origin and of the internal inflection point collapse and that increasing  $h/\Delta S$  further separates those two locations leading to a fully *dense* canopy flow regime.

The internal and the canopy-tip inflection points are common features of the mean velocity profiles obtained with the frontal solidity values considered in this work. The outer inflection point is a direct consequence of the drag discontinuity at the tip of the canopy. The inner inflection point arises as a consequence of the merging of a convex, boundary layer profile in the region close-to-the-bed to a concave shape characterising the mean velocity profile underneath the canopy tip. An upper bound of the location of the inner inflection point can be estimated by assuming that the flow in the canopy resembles the one obtained by a set of jets of diameter  $\Delta S - d$  impinging on the bed. This similarity, inspired by the canopy high wall-normal permeability, suggests that this array of jets would generate a boundary layer by the bed where the impermeability condition must be met. In this scenario, the induced mean streamwise (i.e.,  $x$ ) velocity would present an inflectional point at a distance from the wall of  $y_{int} \simeq 0.4\phi$  ( $\phi$  being the diameter of the jet, see Banyassady & Piomelli 2015). Figure 6(a) shows that when increasing the value of the frontal solidity, the location of the internal inflection point quickly saturates. In particular, it turns out that the asymptotic coordinate of the internal inflection point location is at  $y_{int} \simeq 0.4(\Delta S - d)$ .

Since we have shown that it is the signed distance between the virtual origin and the internal inflection point that sets the actual type of canopy flow, an a priori criterion to determine the on-going flow regime can be put forward by using the above estimates. In particular, since  $h - (\Delta S - d)$  is an upper bound for the virtual origin location  $y_{vo}$ , we could predict the onset of a *dense* regime whenever the inequality  $h - (\Delta S - d) > 0.4(\Delta S - d)$  is verified. Equating the two sides of the previous inequality, we also obtain a regime-transition criterion:  $h/(\Delta S - d) = 1.4$ . If the value of  $d/\Delta S$  used in our simulations (see section §3.1) is used in the previous crude estimate, the corresponding  $\lambda$  value is  $\lambda = 0.208$  which is a close approximation to the value  $\lambda = 0.15$  mentioned above.

The spectral analysis of the velocity fluctuations in different regimes has allowed us to highlight a number of differences between the structure of the corresponding velocity fields. These differences are especially remarkable within the canopy region. In dense regimes with a net separation between the virtual origin and the internal inflection point, the flow structure in the close-to-the-bed region is coupled to the external flow only through the sweep and ejection events that are mainly driven by the coherent quasi streamwise vortices that populate the outer flow and the neighbourhood of the canopy edge (Monti *et al.* 2019). In fact, when the outer coherent structures approach the tip of

the canopy, the spanwise coherence of the external flow is shredded by the stems spacings  $\Delta S$ . At the same time, all the streamwise wavelengths larger than  $O(h)$  are also filtered out by the stems. When the canopy is more shallow, it is uniquely its height that sets the size of the high-pass filter that discriminate on the spanwise and streamwise size of the outer eddies allowed inside the canopy.

Apart from the influence of the wall-normal momentum driven by the outer logarithmic structures, the flow inside the canopy is also strongly influenced by the effects of the inflectional instabilities associated to the presence of the two aforementioned inflection points of the mean velocity profile. An analysis of the cospectra of  $\langle u'v' \rangle$  shows the existence of spanwise energetic structures with spanwise and streamwise coherent sizes of the order of the channel height. These large structures are linked to the inflection point at the tip of the canopy and have been reported by several authors in several obstructed turbulent flows such as canopy flows and flows over porous media with various permeability properties. In the particular case of canopy flows, these structures generate localised Kelvin-Helmholtz rollers that travel along the canopy tip further enhancing the wall-normal momentum exchange between the intra-canopy region and the outer flow.

In the case of dense canopies we have reported the existence of another mechanism taking place in the bed region. Here the lower inflection point may trigger a spanwise coherent modulation of the streamwise velocity components. This modulation has an associated streamwise length scale of the order of the distance of the interior inflection point to the bed. Its presence, associated with the effects of the sweep events driven by the outer flow and the canopy tip rollers, induces a diagonal modulation of the spanwise component of the velocity field probably energised by the momentum transfer that must take place at the wall to verify the impermeability condition. To our knowledge, this is the first time that this mechanism, driven by the presence of the internal mean velocity profile inflection point, has been reported in literature.

## Acknowledgements

A portion of this work was inspired by the authors participation at the TRANSEP Research program in Stability, Transition and Control at KTH in June 2018. We thank Dan Henningson for his hospitality and for providing a stimulating environment and the European Research Council for supporting the program. This work used the *ARCHER* U.K. National Supercomputing Service (<http://www.archer.ac.uk>) through the *U.K. Turbulence Consortium* grant EPSRC EP/L000261/1.

B.E. passed away on 7<sup>th</sup> August 2019 before finalisation of the revision of this manuscript. This work is dedicated to his memory.

## REFERENCES

- BAILEY, B.N. & STOLL, R. 2013 Turbulence in sparse, organized vegetative canopies: a large-eddy simulation study. *Boundary-Layer Meteorology* **147** (3), 369–400.
- BAILEY, B.N. & STOLL, R. 2016 The creation and evolution of coherent structures in plant canopy flows and their role in turbulent transport. *Journal of Fluid Mechanics* **789**, 425–460.
- BANYASSADY, R. & PIOMELLI, U. 2015 Interaction of inner and outer layers in plane and radial wall jets. *Journal of Turbulence* **16** (5), 460–483.
- BELCHER, S.E., JERRAM, N. & HUNT, J.C.R. 2003 Adjustment of a turbulent boundary layer to a canopy of roughness elements. *Journal of Fluid Mechanics* **488**, 369–398.
- BEN MEFTAH, M., DE SERIO, F. & MOSSA, M. 2014 Hydrodynamic behavior in the outer shear layer of partly obstructed open channels. *Physics of Fluids* **26** (6), 065102.

- BEN MEFTAH, M. & MOSSA, M. 2013 Prediction of channel flow characteristics through square arrays of emergent cylinders. *Physics of Fluids* **25** (4), 045102.
- BRÜCKER, C. & WEIDNER, C. 2014 Influence of self-adaptive hairy flaps on the stall delay of an airfoil in ramp-up motion. *Journal of Fluids and Structures* **47**, 31–40.
- DRAZIN, P.G. & REID, W.H. 1981 *Hydrodynamic stability*. Cambridge University Press.
- FADLUN, E.A., VERZICCO, R., ORLANDI, P. & MOHD-YUSOF, J. 2000 Combined immersed-boundary finite-difference methods for three-dimensional complex flow simulations. *Journal of Computational Physics* **161** (1), 35–60.
- FAVIER, J., REVELL, A. & PINELLI, A. 2014 A lattice Boltzmann–immersed boundary method to simulate the fluid interaction with moving and slender flexible objects. *Journal of Computational Physics* **261**, 145–161.
- FINNIGAN, J.J. 2000 Turbulence in plant canopies. *Annual Review of Fluid Mechanics* **32** (1), 519–571.
- FINNIGAN, J.J., SHAW, R.H. & PATTON, E.G. 2009 Turbulence structure above a vegetation canopy. *Journal of Fluid Mechanics* **637**, 387–424.
- GARCÍA-MAYORAL, R. & JIMÉNEZ, J. 2011 Hydrodynamic stability and breakdown of the viscous regime over riblets. *Journal of Fluid Mechanics* **678**, 317–347.
- GHSALBERTI, M. & NEPF, H.M. 2002 Mixing layers and coherent structures in vegetated aquatic flows. *Journal of Geophysical Research: Oceans* **107** (C2), 3–1.
- GHSALBERTI, M. & NEPF, H.M. 2004 The limited growth of vegetated shear layers. *Water Resources Research* **40** (7).
- HAMA, F. R. 1954 Boundary layer characteristics over smooth and rough surfaces. *Soc. Nav. Archit. Mar. Eng., Trans.* **62**, 333.
- HOYAS, S. & JIMÉNEZ, J. 2008 Reynolds number effects on the Reynolds-stress budgets in turbulent channels. *Physics of Fluids* **20** (10), 101511.
- ITOH, M., IGUCHI, R., YOKOTA, K., AKINO, N., R., HINO & S., KUBO 2006 Turbulent drag reduction by the seal fur surface. *Physics of Fluids* **18** - 065102.
- JIMÉNEZ, J. 2004 Turbulent flows over rough walls. *Annual Review of Fluid Mechanics* **36**, 173–196.
- JIMÉNEZ, J. 2013 Near-wall turbulence. *Physics of Fluids* **25** (10), 101302.
- JIMÉNEZ, J. 2018 Coherent structures in wall-bounded turbulence. *Journal of Fluid Mechanics* **842**, 1–100.
- JIMÉNEZ, J., UHLMANN, M., PINELLI, A. & KAWAHARA, G. 2001 Turbulent shear flow over active and passive porous surfaces. *Journal of Fluid Mechanics* **442**, 89–117.
- KIM, J. & MOIN, P. 1985 Application of a fractional-step method to incompressible Navier-Stokes equations. *Journal of Computational Physics* **59** (2), 308–323.
- KIM, J., MOIN, P. & MOSER, R. 1987 Turbulence statistics in fully developed channel flow at low Reynolds number. *Journal of Fluid Mechanics* **177**, 133–166.
- LECLERCQ, T. & DE LANGRE, E. 2016 Drag reduction by elastic reconfiguration of non-uniform beams in non-uniform flows. *Journal of Fluids and Structures* **60**.
- LEONARD, A. 1975 Energy cascade in large-eddy simulations of turbulent fluid flows. *Advances in Geophysics* **18**, 237–248.
- LEONARDI, S., ORLANDI, P. & ANTONIA, R. A. 2007 Properties of d- and k-type roughness in a turbulent channel flow. *Physics of Fluids* **19** (12), 125101.
- LIGHTBODY, A.F. & NEPF, H.M. 2006 Prediction of velocity profiles and longitudinal dispersion in salt marsh vegetation. *Limnology and Oceanography* **51** (1), 218–228.
- LODISH, H., BERK, A. & KAISER, C.A. 2007 *Molecular cell biology*. W.H. Freeman & Co. Ltd.
- LUHAR, M., ROMINGER, J. & NEPF, H.M. 2008 Interaction between flow, transport and vegetation spatial structure. *Environmental Fluid Mechanics* **8** (5-6), 423.
- MARS, R., MATHEW, K. & HO, G. 1999 The role of the submergent macrophyte *triglochin huegelii* in domestic greywater treatment. *Ecological Engineering* **12** (1), 57–66.
- MONTI, A., OMIDYEGANEH, M. & A., PINELLI 2019 Large eddy simulation of of an open-channel flow bounded by a semi-dense rigid filamentous canopy: scaling and flow structure. *Physics of Fluids* **31** (065108).
- NEPF, H.M. 2012 Flow and transport in regions with aquatic vegetation. *Annual Review of Fluid Mechanics* **44**, 123–142.

- NEPF, H.M. & VIVONI, E.R. 2000 Flow structure in depth-limited, vegetated flow. *Journal of Geophysical Research: Oceans* **105** (C12), 28547–28557.
- NEZU, I. & SANJOU, M. 2008 Turbulence structure and coherent motion in vegetated canopy open-channel flows. *Journal of Hydro-Environment Research* **2** (2), 62–90.
- NIKORA, V., MCEWAN, I., MCLEAN, S., COLEMAN, S., POKRAJAC, D. & WALTERS, R. 2007 Double-averaging concept for rough-bed open-channel and overland flows: Theoretical background. *Journal of Hydraulic Engineering* **133** (8), 873–883.
- NIKURADSE, J. 1933 Strömungsgesetze in rauhen röhren. *VDI Forschungsshaft* (361), English translation: NACA-TM 1292 (1950).
- OMIDYEGANEH, M. & PIOMELLI, U. 2011 Large-eddy simulation of two-dimensional dunes in a steady, unidirectional flow. *Journal of Turbulence* (12), N42.
- OMIDYEGANEH, M. & PIOMELLI, U. 2013a Large-eddy simulation of three-dimensional dunes in a steady, unidirectional flow. Part 1. turbulence statistics. *Journal of Fluid Mechanics* **721**, 454–483.
- OMIDYEGANEH, M. & PIOMELLI, U. 2013b Large-eddy simulation of three-dimensional dunes in a steady, unidirectional flow. Part 2. flow structures. *Journal of Fluid Mechanics* **734**, 509–534.
- PERRY, A. E., SCHOFIELD, W.H. & JOUBERT, P.N. 1969 Rough wall turbulent boundary layers. *Journal of Fluid Mechanics* **37** (2), 383–413.
- PINELLI, A., NAQAVI, I.Z., PIOMELLI, U. & FAVIER, J. 2010 Immersed-boundary methods for general finite-difference and finite-volume Navier–Stokes solvers. *Journal of Computational Physics* **229** (24), 9073–9091.
- PIOMELLI, U., ROUHI, A. & GEURTS, B.J. 2015 A grid-independent length scale for large-eddy simulations. *Journal of Fluid Mechanics* **766**, 499–527.
- POGGI, D., PORPORATO, A., RIDOLFI, L., ALBERTSON, J.D. & KATUL, G.G. 2004 The effect of vegetation density on canopy sub-layer turbulence. *Boundary-Layer Meteorology* **111** (3), 565–587.
- RAUPACH, M.R., FINNIGAN, J.J. & BRUNEI, Y. 1996 Coherent eddies and turbulence in vegetation canopies: the mixing-layer analogy. *Boundary-Layer Meteorology* **78** (3-4), 351–382.
- RAUPACH, M.R. & SHAW, R.H. 1982 Averaging procedures for flow within vegetation canopies. *Boundary-Layer Meteorology* **22** (1), 79–90.
- RHIE, C.M. & CHOW, W.L. 1983 Numerical study of the turbulent flow past an airfoil with trailing edge separation. *AIAA Journal* **21** (11), 1525–1532.
- ROSTI, M.E., OMIDYEGANEH, M. & PINELLI, A. 2016 Direct numerical simulation of the flow around an aerofoil in ramp-up motion. *Physics of Fluids* **28** (2), 025106.
- ROUHI, A., PIOMELLI, U. & GEURTS, B.J. 2016 Dynamic subfilter-scale stress model for large-eddy simulations. *Physical Review Fluids* **1** (4), 044401.
- SCHLICHTING, H. 1936 Experimentelle Untersuchungen zum Rauigkeitsproblem. *Archive of Applied Mechanics* **7** (1), 1–34.
- SCHULTZ, M.P. & FLACK, K.A. 2009 Turbulent boundary layers on a systematically varied rough wall. *Physics of Fluids* **21** (1), 015104.
- SCOTTI, A. 2006 Direct numerical simulation of turbulent channel flows with boundary roughened with virtual sandpaper. *Physics of Fluids* **18** (3), 031701.
- SHARMA, A. & GARCÍA-MAYORAL, R. 2018 Scaling and modelling of turbulent flow over a sparse canopy. *arXiv preprint arXiv:1810.10028* .
- SHIMIZU, Y., TSUJIMOTO, T., NAKAGAWA, H. & KITAMURA, T. 1991 Experimental study on flow over rigid vegetation simulated by cylinders with equi-spacing. *Doboku Gakkai Ronbunshu* **1991** (438), 31–40.
- TANI, I. 1987 Turbulent boundary layer development over rough surfaces. In *Perspectives in turbulence studies*, pp. 223–249. Springer.
- TUERKE, F. & JIMÉNEZ, J. 2013 Simulations of turbulent channels with prescribed velocity profiles. *Journal of Fluid Mechanics* **723**, 587–603.
- WEBB, R.L., ECKERT, E.R.G. & GOLDSTEIN, R.J. 1971 Heat transfer and friction in tubes with repeated-rib roughness. *International Journal of Heat and Mass Transfer* **14** (4), 601–617.
- WILCOCK, R.J., CHAMPION, P.D., NAGELS, J.W. & CROKER, G.F. 1999 The influence of

- aquatic macrophytes on the hydraulic and physico-chemical properties of a New Zealand lowland stream. *Hydrobiologia* **416**, 203–214.
- YANG, U.M. & OTHERS 2002 Boomerang: a parallel algebraic multigrid solver and preconditioner. *Applied Numerical Mathematics* **41** (1), 155–177.
- YUAN, J. & PIOMELLI, U. 2014 Roughness effects on the reynolds stress budgets in near-wall turbulence. *Journal of Fluid Mechanics* **760**.